Simulation of negative-streamer dynamics in nitrogen

P. A. Vitello, B. M. Penetrante, and J. N. Bardsley
High Temperature Physics Division, Lawrence Livermore National Laboratory, Livermore, California 94550
(Received 4 August 1993)

In this paper we consider how the dynamical characteristics of streamers are determined by their multidimensional structure. Results from two-dimensional (three-dimensional, cylindrically symmetric) simulations are presented at atmospheric pressure for N_2 and plane-parallel electrodes. Our high-spatial-resolution simulations are based on a numerical model which is able to treat a wide range of electrode configurations (including point-to-plane and other complex configurations). This model has allowed us to make a more thorough investigation of streamer morphology than has been attempted previously. Detailed knowledge of the streamer morphology and its evolution are vital to the application of streamer discharges to processes such as the destruction of airborne toxic chemicals. We find that the morphology is complex, even for plane-parallel electrodes, with a range of radial structures that become evident at different phases of the streamer evolution. Several distinct phases of evolution are clearly discernible. We demonstrate the transition between these phases, showing how the self-consistent radial and axial structure varies with time.

PACS number(s): 52.80.Mg, 51.50.+v

I. INTRODUCTION

Streamers are transient filamentary plasmas whose dynamics are controlled by highly localized nonlinear space-charge waves. Streamers have been observed in gases [1–5], in transformer oils and other fluids [6–8], and even in semiconductors [9]. At present there is lacking a realistic theoretical model of streamers that would describe the dependence of the parameters of the streamer on the applied voltage, on the electrode geometry and polarity, and on the other physical characteristics of the propagating medium. There has been an increased interest in the dynamics of streamers in gases because of their application to the removal of air-borne toxic chemicals [10–12]. In this application, the streamers produce energetic electrons that, through dissociation and ionization processes, generate active radicals. The radicals diffuse through the gas and then react with toxic molecules. Devices employing streamers for plasma-catalytic chemical reactions show high power efficiency because, within the short lifetime of the streamer, the ions do not experience significant movement and therefore do not contribute to the power consumption. The short lifetime of the streamers is implemented with the use of very short high-voltage pulses and/or with the use of dielectric coatings on the electrodes.

The morphology of streamers determines in large part the energy distribution of the high energy electrons produced during the discharge. The electron distribution function that results from a streamer discharge is highly nonlinear with respect to energy, due to the existence of very strong space-charge fields, but typically is in near equilibrium with the field [13–15]. Detailed knowledge of the temporal and spatial evolution of the densities, and of the space-charge fields in the streamer is required to determine the total electron energy distribution. An understanding of the fast electron distribution is vital to the control and optimization of air-borne toxic process efficiencies because of the strong energy dependence of the atomic rates.

If the streamer is initiated from a small, localized enhancement to the background neutral plasma density (containing a single or a few electrons), then the first phase of growth is a diffusion dominated avalanche of electrons drifting in the unperturbed background electric field. A streamer will form if the amplification in this avalanche is sufficiently large to produce strong self-fields and self-shielding before the drifting electrons reach the anode. Such streamers form a double headed filament containing both positive (cathode directed) and negative (anode directed) streamer components. We term this regime the avalanche phase (AP) of streamer development. Assuming single-electron avalanche initiation and a homogeneous applied field, Raether [1] predicted that streamer initiation would occur after the avalanche had traversed a critical distance given by $z_{cr} \simeq 20/\alpha$, where α is the electron impact ionization coefficient. If the initial density enhancement is sufficiently high that it can provide self-shielding without the need for density enhancements via further ionization (i.e., the Debye length in the density perturbation is small compared with its size), then the weak space-charge field AP is bypassed, and the nonlinear space-charge field phase begins immediately (see Vitello, Penetrante, and Bardsley [15]). For high density initial perturbations, a single streamer head tends to form if the perturbation is placed adjacent to an electrode. A double headed streamer similar to that formed from an avalanche will develop if the initial high density perturbation is placed between the electrodes. We focus in this paper on single headed negative streamers, showing that their structure is essentially the same as that of the negative streamer component of double headed streamers.

In a streamer, rapid ionization takes place in the high space-charge field region about the streamer head due to collisions between electrons and the background neutrals.

For negative streamers the ionizing electrons are accelerated outwards by the space-charge fields, extending the streamer towards the anode. These strongly accelerated electrons can be electrons which have been pushed out of the streamer body by the space-charge field or diffusion, or by electrons produced by any other means, such as preionization. Preionization or the operation of some other nonlocal mechanism for creating free electrons ahead of the streamer, such as photoionization or ionization from runaway electrons [16], is not necessary for the propagation of negative streamers, but serves to modify their structure [15], and in some cases may guide the streamer propagation [17]. In a positive streamer the electrons in the enhanced field region of the streamer head are accelerated inwards, into the streamer body. These electrons must be produced by some external mechanism [18]. Runaway electrons produced in the high field region of a positive streamer head would be accelerated into the streamer and hence would be less likely than preionization or photoionization to contribute to the positive streamer propagation.

Streamers show a complex radial morphology which changes with time as the streamer develops. The radius structure cannot simply be described by a single radial length scale. Early streamer models [19,20] assumed that simple electron diffusion was the dominant process determining the streamer radius. Unipolar diffusion does dominate the radial expansion of an avalanche as long as the space-charge fields are negligible. The dominance of diffusion ends when the electron drift velocity due to the avalanche space-charge field becomes larger than the diffusion expansion rate [21,22]. When this occurs the streamer enters what we term the space-charge phase (SCP). During this transitional phase, which comes before a true filamentary structure forms, there can be a rapid change in the radius of the streamer head. Depending upon initial conditions the radius expands or contracts during this phase to a self-consistent streamer radius. After the SCP, streamers may propagate for considerable distances with slow variations in their radius, producing long filamentary regions of high electron density. This filamentary regime of streamer propagation we call the filamentary streamer phase (FSP). The channel formed during the FSP is quasineutral and of density $\simeq 10^{14}$ cm^{-3} for the conditions considered in this paper. Because of the low ion drift velocity, roughly 1/100th of the electron drift velocity for N_2, and the low ionization rate interior to the streamer, the high density spatial structure of the streamer body changes very slowly with time during this phase.

Depending upon the preionization value and background electric field magnitude, the FSP may be followed by a renewed phase of rapid expansion, which we call the expansion streamer phase (ESP) [15]. The ESP was observed to occur for both negative and positive streamers and leads to the transition from a filamentary discharge to an extended diffuse discharge. We consider in this paper a low preionization density for which the ESP does not occur. A detailed study of the transition from the FSP to the ESP will be considered in a forthcoming paper.

Models of streamers based on a fluid treatment of the electrons and ions have recently been developed. The comparison by Wu and Kunhardt [23] of Monte Carlo and fluid equation treatments of streamer formation and propagation has demonstrated the validity of the fluid treatment in modeling streamers. Streamers are multidimensional phenomena. The importance of the multidimensional nature of the space-charge distribution and its corresponding electric field was pointed out by Davies and Evans [24]. Even for simple one-dimensional (1D) streamer modeling, where the radius and radial structure are assumed, one must use a multidimensional model to correctly calculate the electric field. A number of approaches have been used to approximate the space-charge field in more than one dimension. In the early work of Davies, Davies, and Evans [25] the solution of Poisson's equation was based on the representation of a space-charge filament by a series of charged disks of equal radii, with a given uniform space-charge density in each disk. For a positive streamer the radius was determined from the assumption that unipolar diffusion dominated the radial expansion of electrons moving towards the streamer head until the space-charge fields became nonlinear and halted further expansion [19]. Estimates for positive streamer radii could only be made from this model. Using the method of disks the value of the electric field on the streamer axis was then calculated. Many workers have adopted the disk method field solver and the diffusion estimate for the streamer radius in conjunction with 1D dynamics simulations [25–31] and even low resolution two-dimensional (2D) simulations [32]. An improvement over the constant radial density profile was introduced by Gallimberti [13], who used a Gaussian radial density profile. As the peak space-charge field, and hence the highest energy electrons are produced at the streamer head, its structure is of great importance in modeling streamers. In 1D simulations the assumption of a fixed radius leads to a flat headed streamer, and precludes self-consistent studies of its evolution. The earlier 1D models, which neglected space-charge effects [19,20], treated the streamer head as being spherical, but were generally less self-consistent than the constant radius fluid models. More recent 1D models have considered streamers capped by a conical spheroid, hyperboloid, or ellipsoid [21,33]. These rounded head models improved the self-consistency of 1D streamer simulations, but are still far from adequate as the radius and the radius of curvature of the streamer head were not self-consistently calculated.

To determine self-consistently the radial structure of streamers, multidimensional modeling is required. The 2D simulations which were published previously have been restricted to low-spatial-resolution plane-parallel electrode configurations [14,23,32,34–41]. These models typically used a grid spacing with axial and radial resolution of >25 μm and >50 μm, respectively. We find in our 2D modeling, in agreement with the 1D modeling of Morrow [30], that this resolution is inadequate to accurately determine either the axial or radial structure of streamers due to their extremely steep, shocklike density and electric field gradients, which characterize the boundary separating the streamer and the background

plasma.

To study the radial and axial structure of streamers, we have developed a 2D simulation model with spatial resolution of $\lesssim 5\ \mu$m that can be applied to arbitrarily shaped electrode structures. Following Dhali and Williams [37,38], we neglect photoionization and possible runaway electron effects and propagate our streamers through a preexisting low ionization N_2 plasma. We take this approach partly to make our high resolution modeling more tractable, but also owing to the fact that the present knowledge of the significance and even the mechanism for photoionization in N_2 are poorly understood [21]. In addition, runaway electrons are not expected for E/N magnitudes at the streamer head below 1500 Td (townsends) [42,43]. We have used our 2D model to study the multidimensional evolution of the structure and propagation of streamers for plane-parallel and highly nonuniform point-to-plane applied fields. We find that the streamer morphology is complex even in the plane-parallel case in N_2, with a range of radial structures which become prominent at different phases of the streamer evolution. The transition between these phases is discussed in this paper for plane-parallel electrodes, showing how the self-consistent radial and axial structure varies with time. The major objective of this paper is to demonstrate how the dynamical characteristics of streamers are determined by their multidimensional structure. Our high-spatial-resolution simulations have allowed us to make a more thorough investigation of the streamer morphology than has been attempted previously. To this end we do not attempt to compare our calculations with specific experimental results, leaving this to a further study once the physics of streamer evolution is better understood.

In Sec. II, the simulation model is discussed. Numerical techniques are considered in Sec. III. The results of our calculations are presented, and concluding remarks are given in Sec. IV.

II. SIMULATION MODEL

The simulation of the development of a streamer using a kinetic description such as a Monte Carlo simulation or a space-time-dependent Boltzmann transport solution is numerically very time consuming [39]. An alternate self-consistent description, using moment equations, is highly desirable in order to make streamer modeling tractable computationally. The question arises as to the number of moments that need to be used to describe the development of the streamer, and how to determine the various transport and reaction rate coefficients that appear in their equation of evolution. At near atmospheric densities, the momentum and energy equilibration time and distance scales are small compared to any macroscopic scale variations of the system, and a single moment description using the continuity equation for the various particle densities is satisfactory [15,44].

The basic dynamical equations for streamer formation and propagation therefore are the continuity equations for electrons and ions. The electric field is solved using Poisson's equation. These equations take the form

$$\frac{\partial n_e}{\partial t}+\nabla\cdot n_e\mathbf{v}_e-\nabla\cdot\mathbf{D}_e\cdot\nabla n_e=|\mathbf{v}_e|(\alpha-\eta)n_e+S\ , \tag{1}$$

$$\frac{\partial n_p}{\partial t}+\nabla\cdot n_p\mathbf{v}_p=|\mathbf{v}_e|\alpha n_e+S\ , \tag{2}$$

$$\frac{\partial n_n}{\partial t}+\nabla\cdot n_n\mathbf{v}_n=|\mathbf{v}_e|\eta n_e\ , \tag{3}$$

$$\nabla^2\phi=-e(n_p-n_e-n_n)/\epsilon_0\ , \tag{4}$$

where n_e, n_p, and n_n are the electron, positive-ion, and negative-ion densities, respectively, $\mathbf{v}_e$, $\mathbf{v}_p$, and $\mathbf{v}_n$ are the corresponding drift velocities, η is the attachment coefficient, $\mathbf{D}_e$ is the electron diffusion coefficient tensor, ϕ is the electric potential, e is the electric charge, and ϵ_0 is the permittivity of free space. In the following, we define the space-charge density n_s as

$$n_s\equiv n_p-n_e-n_n\ . \tag{5}$$

Ion diffusion is unimportant for cold ions (which we assume in our modeling) and for the time scales of interest in our calculations. The source term S describes the effects of any of several particle source and sink mechanisms such as photoionization. We have not included such mechanisms in the calculations presented here, and present results here for N_2 with $S=0$, $\eta=0$, and $n_n=0$.

In modeling streamers we assume that the electron and ion densities can be calculated using the continuity equations (1)–(3), and that the drift velocities and the electron impact ionization coefficient α are functions of E/P, where the electric field magnitude is in V/cm and the pressure P is in units of Torr. For N_2, we use the values of α and the electron and positive-ion mobilities (μ_e,μ_p) given by Davies, Davies, and Evans [25] and Dhali and Williams [38],

$$\alpha=5.7Pe^{-260P/E}\ (\mathrm{cm}^{-1})\ , \tag{6}$$

$$\mu_e=2.9\times10^5/P\ (\mathrm{cm}^2/\mathrm{Vs})\ , \tag{7}$$

$$\mu_p=2.6\times10^3/P\ (\mathrm{cm}^2/\mathrm{Vs})\ . \tag{8}$$

The transverse and the longitudinal diffusion coefficients $D_{e_{zz}}=1800\ \mathrm{cm}^2/\mathrm{s}$ and $D_{e_{zz}}=2190\ \mathrm{cm}^2/\mathrm{s}$ [1,45] are valid for N_2 at 760 Torr and were assumed to scale as $1/P$. We make use in our analysis of the following definitions for the electron velocity due to diffusion $\mathbf{v}_D$, the total electron velocity $\mathbf{v}_T$, the electron drift velocity $\mathbf{v}_e$, and the electron drift velocity in the background electric field $\mathbf{v}_B$:

$$\mathbf{v}_D\equiv\frac{-\mathbf{D}_e\cdot\nabla n_e}{n_e}\ , \tag{9}$$

$$\mathbf{v}_e\equiv-\mu_e\mathbf{E}\ , \tag{10}$$

$$\mathbf{v}_T\equiv\mathbf{v}_e+\mathbf{v}_D\ , \tag{11}$$

$$\mathbf{v}_B\equiv-\mu_e\mathbf{E}_B\ , \tag{12}$$

where $\mathbf{E}_B$ is the background vacuum electric field.

The rates used assume that a local equilibrium with the background neutral plasma is achieved for the electron distribution function at pressure P in the electric field of

magnitude E. This is valid as long as the relaxation time for achieving a steady state electron energy distribution function is short compared to the characteristic time of discharge development. The electron relaxation time can be calculated by solving the Boltzmann equation, which describes the time evolution of the electron energy distribution function.

In this study we are primarily interested in investigating self-consistent, multidimensional development and propagation of streamers. We find that even for the simplest geometry a complex morphology exists. In order to reduce the complexity of streamer propagation we have therefore not included the photoionization source term or explicit secondary emission at the cathode, and discuss here only discharges between plane-parallel plates. We follow the work of Dhali and Williams [37,38] in using as our initial background condition a uniform partially ionized neutral plasma of density n_B. The streamer growth was initiated by the addition to the uniform background plasma of a spherical neutral plasma density component having a Gaussian distribution with maximum density n_G and $1/e$ radius r_G. We have considered a broad range of enhanced densities with our model (see Vitello, Penetrante, and Bardsley [15]), but will discuss here only high density initial perturbations which bypass the AP and immediately enter the SCP. We wish to stress that our high-spatial resolution allows us to present the first detailed treatment of the growth of streamers from perturbations much smaller than the final streamer radius.

With our grid spacing we were unable to resolve the cathode-fall region close to the cathode. Instead we use as the boundary condition on the cathode the requirement that the conduction current be continuous. By comparing the results of single negative streamer growth (initialized by high density perturbations at the cathode) with double headed streamer growth (initialized by high density perturbations between the electrodes) we find that our model results are insensitive to our neglect of the cathode-fall region and our assumption of current continuity.

III. NUMERICAL MODEL

The continuity equations (1)–(3) were solved numerically using a finite difference scheme in cylindrically symmetric coordinates (r,z). We used the multidimensional flux-corrected transport (FCT) scheme developed by Zalesak [46]. FCT schemes have been successfully used [23,30,38] to accurately treat the very sharp gradients and large dynamic range encountered at the surfaces of streamers. We use a modified form of the numerical differencing scheme described by Dhali and Williams [38] in treating the continuity equations. For cylindrically symmetric coordinates the convective terms in the continuity equations (1)–(3) can be written as

$$\left.\frac{\partial N}{\partial t}\right|_{\text{conv}} = -\frac{1}{r}\frac{\partial f}{\partial r} - \frac{\partial g}{\partial z} , \tag{13}$$

where N here corresponds to either n_e, n_p, or n_n, $f \equiv rNv_r$, and $g \equiv Nv_z$. In our calculations we use a 2D spatial grid of points. Densities and the electric potential are evaluated at the centers of our grid, with the density $N_{i,j}$ corresponding to the density at the ith radial and jth axial grid point. Velocities are evaluated at the grid boundaries. The grid is spaced such that the inner boundary of the first radial grid point lies on the axis and the last radial grid point lies at the outer boundary at distance $R_{\max}$ from the axis. Similarly we place the inner boundary of the first axial grid point at the anode, and the outer boundary of the last axial grid point at the cathode at $Z_{\max}$. We use finite difference equations to solve Eq. (13). At time t we assume that all physical quantities are known. Our convective difference scheme, which uses a half step in time and then a full step to achieve second order temporal accuracy, can be described by

$$N_{i,j}^{t+\delta t/2} = N_{i,j}^{t} - \frac{\delta t}{2V_{i,j}}\left(F_{i+1/2,j}^{t} - F_{i-1/2,j}^{t} + G_{i,j+1/2}^{t} - G_{i,j-1/2}^{t}\right) , \tag{14}$$

$$N_{i,j}^{t+\delta t} = N_{i,j}^{t} - \frac{\delta t}{V_{i,j}}\left(F_{i+1/2,j}^{t+\delta t/2} - F_{i-1/2,j}^{t+\delta t/2} + G_{i,j+1/2}^{t+\delta t/2} - G_{i,j-1/2}^{t+\delta t/2}\right) , \tag{15}$$

where δt is the time step, $V_{i,j} = r_i \Delta r_i \Delta z_j$, $\Delta r_i = r_{i+1/2} - r_{i-1/2}$, $\Delta z_j = z_{j+1/2} - z_{j-1/2}$, and $F \equiv r\Delta z N u_r$ and $G \equiv r\Delta r N v_z$ correspond respectively to the fluxes at the grid boundaries. In calculating the fluxes F and G, the grid boundary velocities are calculated as

$$v_{r_{i+1/2,j}} = -q\mu\frac{(\phi_{i+1,j} - \phi_{i,j})}{(r_{i+1} - r_i)} , \tag{16}$$

$$v_{z_{i,j+1/2}} = -q\mu\frac{(\phi_{i,j+1} - \phi_{i,j})}{(z_{j+1} - z_j)} , \tag{17}$$

where $q = \pm$, with the sign depending upon whether electrons, negative ions, or positive ions are being considered. We used second order centered spatial interpolation to determine the density at the cell boundary for use in evaluating F and G, except in the region of the steepest density gradient, where second order upwind spatial interpolation was used. The upwind differencing stabilized the development of the positive streamer head where the ionization wave motion runs counter to the electron velocity. The small amount of numerical diffusion inherent in the second order fluxes was found to be beneficial in that it damped numerically induced space-charge oscillations caused by our imperfect resolution of the extremely thin space-charge layer at the streamer head. These oscillations, if not damped, were found to grow into nonlinear waves which lead to branching of the streamer head. In general we found that the streamer head was at best neutrally stable to perturbations. The use of third order or higher numerical schemes everywhere resulted in the propagation and amplification of numerical noise.

The diffusion term in the electron continuity equation (1) was time split and solved using an alternating direction implicit (ADI) technique which was second order accurate in time and in space [47]. An implicit method for the diffusion term was found necessary to avoid time step

limitations and/or numerical instabilities which arose when very fine grid spacing was used. The effects of the ionization and attachment terms were also time split and solved to second order in time using a half-step, full time step scheme.

For the calculations presented here we used a spatial mesh which was uniform in z, but nonlinear in r. For the radial coordinate, the mesh was uniform for $0<r<r_m$, and stretched from $r_m<r<R_{\max}$, where $R_{\max}\gg r_m$. The outer radial boundary $R_{\max}$ was chosen to be sufficiently large so that the radial boundary conditions of the electric potential did not affect the electric field at radii near the streamer. Typically, $R_{\max}$ was chosen to be at least equal to the gap between the plane-parallel electrodes. The radius r_m was similarly chosen to be much larger than the streamer radius to allow for a uniform grid over the entire streamer volume.

The potential field was calculated by solving Poisson's equation (4). In calculating ϕ, we used a numerical iterative solver which alternated between the strongly implicit (SIP) scheme developed by Stone [48] and the successive over relaxation (SOR) scheme. The SIP scheme was used every fourth time step, with the SOR scheme being used for all other time steps. A discussion of the merits of these schemes for solving Poisson's equation is given by Vitello, Cerjan, and Braun [49]. Generally the SOR scheme converges much more slowly than does the SIP scheme, but takes less computer time per iteration. As the potential changes slowly over a given time step during our calculations, the SOR scheme converged to a small fractional change in potential (less than 10^{-5} per iteration) quite rapidly. This small fractional change per iteration can be misleading as the decrease in the fractional change per iteration is very slow for the SOR scheme. The SIP solver was used to correct for possible error introduced by the SOR convergence difficulties. The SIP scheme is much slower per iteration, but shows both very rapid convergence and a rapid decrease in the fractional change per iteration during convergence. The combined scheme proved to be very effective, combining high global accuracy of the SIP scheme with the speed of the SOR scheme.

For the potential, we used symmetric boundary conditions in r at the origin and at the outer radius $R_{\max}$. Although our model can treat time variations in the electrode voltages, for the calculations presented here we held the potential fixed in time. Our Poisson solver was designed to include interior boundary conditions of fixed potential points to allow treatment of arbitrary spatial structured electrodes [49]. Simulations of a point-to-plane streamer discharge using this model was presented by Vitello, Penetrante, and Bardsley [15].

For stability and accuracy the time step in our calculations was limited by several considerations. The time scales of relevance are the Courant, effective ionization, and dielectronic relaxation time scales, which are given respectively by

$$\delta t_C=\min\left[\sum_{i,j}\frac{\Delta r_i}{v_{r_{i,j}}},\frac{\Delta z_j}{v_{z_{i,j}}}\right], \tag{18}$$

$$\delta t_I=\min\left[\sum_{i,j}\frac{1}{|\alpha_{i,j}-\eta_{i,j}||\mathbf{v}_e|}\right], \tag{19}$$

$$\delta t_D=\min\left[\sum_{i,j}\frac{\epsilon_0}{e\mu_e n_e}\right]. \tag{20}$$

The model time step was calculated as $\delta t=\min(A_C\delta t_C, A_I\delta t_I, A_D\delta t_D)$, with $A_C=0.5$, $A_I=0.1$, and $A_D=0.5$.

IV. RESULTS

Streamers have a complex poorly understood morphology, even for the simple plane-parallel electrode geometry. We therefore restrict ourselves to a limited set of conditions, considering primarily the rapid growth of negative streamers between plane-parallel plates from a high density axially symmetric Gaussian perturbation at the cathode. We restrict our temporal study of the streamers to the period of the first streamer transit between the electrodes after the time of perturbation. This work is similar to the modeling done by Dhali and Williams [37,38], but uses much higher spatial resolution. We find agreement with many of the results of earlier, lower resolution simulations, but our studies also reveal many differences. The gap spacing, unless explicitly stated otherwise, was 0.5 cm, with 1000 uniform grid points in z. The radial grid was uniform between the origin and $r_m=0.1$ cm, with 200 points, and stretched from r_m and $R_{\max}=0.5$ cm using an additional 100 grid points. This gives a 5-μm resolution over the streamer volume. For most of the data presented here the voltage was held fixed at 25 kV, which corresponded to an electric field magnitude of approximately 40% overvoltage for N_2 at atmospheric pressure.

We begin our study by considering streamer development from a perturbation centered on the cathode with $r_G=25$ μm, $n_G=10^{14}$ cm^{-3}, and $n_B=1$ cm^{-3}. For this low background and high perturbation density a narrow streamer filament rapidly develops. The streamer radius expands during the SCP phase, and then propagates across the electrode gap with nearly constant radius during the FSP, leaving behind a channel of high density ($n_e\simeq 10^{14}$ cm^{-3}) plasma.

A. Negative streamer development

The development of a streamer is a very nonlinear phenomenon. We first discuss the overall evolution. A more detailed investigation of the SCP and the FSP then follows. For the conditions considered, a streamer is launched from the cathode on a nanosecond time scale. In Fig. 1 are shown the axial profiles of n_e and of $|n_s|$. The corresponding profiles of $|E|$ are given in Fig. 2. The SCP covers the period roughly from $t=0$–2 ns and is followed by the FSP. During the FSP, the density gradient at the streamer head steepens until the drop becomes precipitous. As the density gradient steepens, the negative shielding space charge at the streamer head becomes confined to an increasingly thin layer. This shielding surface space charge leads to an electric field similar to that

about a highly conducting needle. It is this excess electron density, which is not tied to the ions, that gives the sharp peak to the electron density profiles at the streamer head in Fig. 1. We describe the streamer as consisting of head, body, and base regions. The streamer head is distinguished by its high space charge and space-charge field, while the streamer body is defined as the filamentary region between the head and the base. After the onset of the FSP the base region continues to grow slowly in the axial direction due to electron drift motion. Details of the 2D evolution of the head, body, and base regions will be considered later in this paper.

The electric field in the streamer body (see Fig. 2) is considerably lower than the background value, but it is still non-negligible. The value of the internal electric field is self-consistently determined by the requirement that the total conduction and induction current through the streamer be constant. At early times current conservation requires a decrease in $|E|$ near the cathode because of the high electron density of the initial perturbation. The decrease in $|E|$ at the base becomes less noticeable as the density in the streamer body increases relative to that in the base. The drop off from the peak electric field to the interior field becomes very sharp as the shielding space-charge layer shrinks in width, but the drop is smooth when this region is well resolved. For our model conditions we find the electric field on axis behind the streamer head to be shielded to a value of $\simeq 30$ kV/cm. The electric field magnitude rises again in the streamer base until its value is $\simeq 43$ kV/cm, which is only slightly lower than the background field of 50 kV/cm.

Except at the surface the streamer plasma is quasineutral, with the electron density being tied to the slow moving ion density so as to reduce the space charge. The space-charge density is negative in the streamer body during the SCP, producing a radial space-charge field which pushes electrons outwards. With time, n_s becomes positive in the streamer body. The onset of a positive value for n_s in the streamer body is one of the structural changes that occurs when the streamer passes from the SCP to the FSP. At the streamer base, n_s remains negative during the FSP. The space-charge density in the streamer body and base varies slowly both in space and in time during the FSP.

As the streamer propagates, the values of n_e, n_s, and $|E|$ all increase at the streamer head for our conditions.

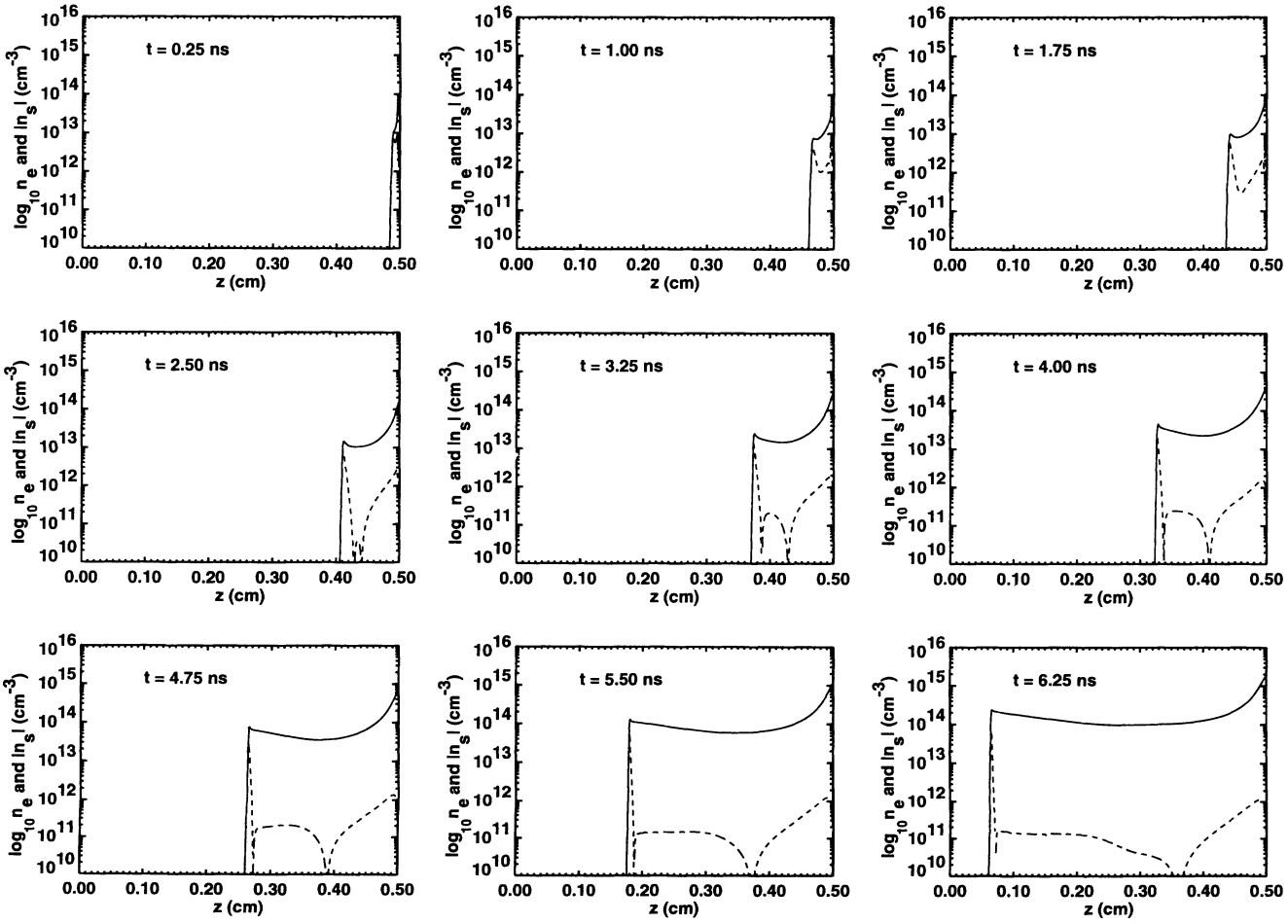

FIG. 1. Evolution of n_e and of $|n_s|$ along the axis. Initial conditions used were plane-parallel gap with separation 0.5 cm, fixed voltage 25 kV, $n_B = 1$ cm^{-3}, $r_G = 25$ μm, and $n_G = 10^{14}$ cm^{-3}. The initial high density Gaussian perturbation is centered at the cathode at $z = 0.5$ cm. The solid, dot-dashed, and dotted lines correspond to n_e, $|n_s|$ for $n_s > 0$ and $|n_s|$ for $n_s < 0$, respectively.

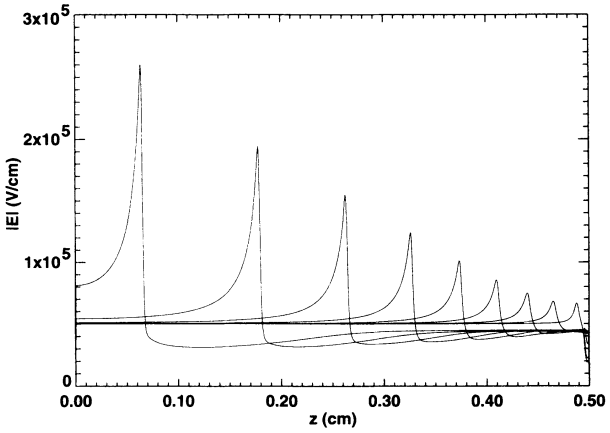

FIG. 2. Evolution of the magnitude of the electric field along the axis. The profiles correspond to the same initial conditions and times as given in Fig. 1.

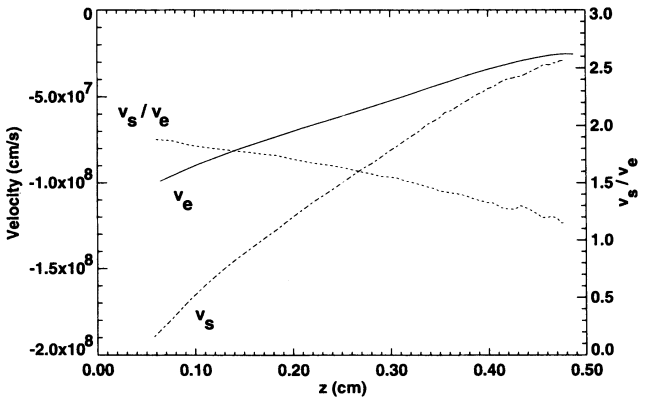

FIG. 4. Time dependence of v_s, the peak value of v_e, and of the ratio of v_s to the peak value of v_e. Note that the velocities v_e and v_s are negative and that their magnitudes increase as the streamer head approaches the origin.

In Fig. 3 are plotted the variations of the peak value of the electron density, the space-charge density, and the electric field magnitude at the streamer head as a function of the streamer head position. The variables are scaled to their values for the streamer head position at $z=0.06$ cm. We define the streamer head position as the axial point where the shielding space-charge density has its maximum magnitude. Also shown is the time history of the streamer propagation velocity v_s. After an initial slow variation in the SCP ($z \gtrsim 0.4$ cm), v_s, n_s, and $|E|$ increase roughly linearly with position until the streamer head approaches the anode. The electron density increases more rapidly. Closer to the anode ($z \lesssim 0.1$ cm) the streamer head experiences an enhancement to its space-charge field due to mirror charges, leading to a more rapid increase with position. The near linear variation of v_s with streamer length implies an exponential time variation of v_s. The ratio of v_s of the peak value of the electron drift velocity v_e (which is proportional to $|E|$) slowly increases during the FSP for the conditions considered (see Fig. 4). As we will show below, the electron diffusion velocity is much smaller than that of the drift velocity except in regions of negligible electron density. Near the anode the streamer propagation speed becomes greater than twice the maximum electron drift velocity. This shows the effect of ionization in enhancing the streamer propagation over the electron drift velocity.

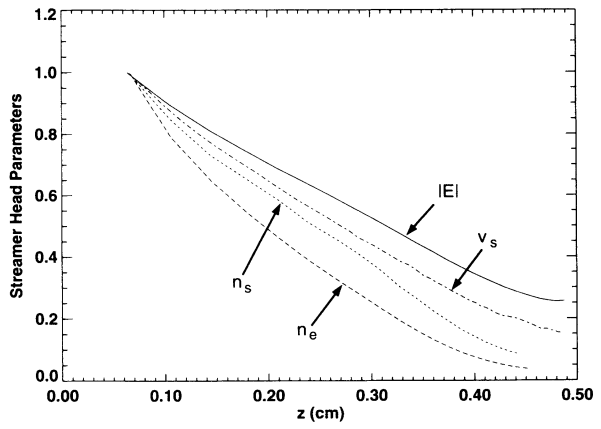

FIG. 3. Scaled axial variation in v_s, and in the peak values of n_e, n_s, and $|E|$ at the streamer head as a function of the streamer head position.

A linear scaling of v_s with streamer length has been observed experimentally for streamers in neon [50,51], and was predicted by Lozansky and Firsov [52] in their analytic model which treated streamers as a moving, perfectly conducting plasma. The velocity at the streamer surface was assumed in their model to be that of the local electron drift velocity. Starting from an initial spherical plasma distribution in a uniform background electric field and assuming cylindrical symmetry, the streamer surface was found to evolve into an ellipsoid of revolution with constant curvature at the streamer head. The result that v_s varies roughly as streamer length follows from the similar variation of $|E|$ at the surface of the conducting plasma for this geometry when the minor axis of the ellipsoid is much smaller than its major axis length. This model, while giving some insight into streamer development, ignores ionization and cannot explain such fundamental features such as why the streamer propagation velocity is much greater than the maximum drift velocity.

For negative streamers the electrons in the streamer head move in the same direction as the streamer propagates. The evolution of the streamer flow field for the total electron velocity is presented in Fig. 5. The flow field shows that $\mathbf{v}_T$ differs significantly from the background velocity only about the streamer head and in the streamer body behind the head. The flow about the head shows strong expansion. In the streamer body, $\mathbf{v}_T$ is reduced below the background velocity due to space-charge shielding and shows a slight inward convergence from the local net positive space charge. At the streamer base there is a slow radial expansion in the flow field, with $\mathbf{v}_T \simeq \mathbf{v}_B$.

In prior low resolution 2D simulation models [23,37–39,41], streamer evolution was often described as going through an initial transition phase and then settling

down into a near-steady-state propagation mode. In our modeling we find that the typical behavior of streamer propagation is anything but steady state. With low-spatial resolution, structural variations due to processes with unresolved length scales cannot develop. We find that high-resolution modeling is essential to allow the streamer structure to self-consistently evolve in space and in time.

B. Space-charge phase

During the AP the electron density expands purely due to diffusion. For a uniform background field and a point charge initial density distribution, the electron density in the avalanche takes the form of a drifting spherical Gaussian distribution [18],

$$n_e(\vec{r},t)=\frac{1}{(4\pi t)^{3/2}D_{e_{rr}}D_{e_{zz}}^{1/2}} \times\exp\left[-\frac{x^2+y^2}{4D_{e_{rr}}}-\frac{(z-|\mathbf{v}_B|t)^2}{4D_{e_{zz}}}+\alpha|\mathbf{v}_B|t\right]. \quad (21)$$

The radial scale length is given by $r_D\equiv(4D_{e_{rr}}t)^{1/2}$. During the AP, n_e grows exponentially, as does the space-charge density, since the ions are left behind unshielded.

For our initial high density perturbations we bypass the AP of streamer growth and begin directly with the SCP. We show that the late time FSP streamer head and body structure are weakly dependent upon our choice of initial perturbation conditions. The evolution of n_e, n_s, v_{T_r}, and $v_{T_z}-v_{B_z}$ during the SCP (which lasts roughly from $t=0$–2 ns for the conditions considered) is shown in Fig. 6. Initially, n_e consists of a purely spherical Gaussian profile plus a constant density, the space-charge density is zero, and the components to $\mathbf{v}_T$ are due to diffusion and the drift velocity in the background electric field. With increasing time, space-charge fields become progressively dominant, enforcing charge neutrality at high densities. The low ion velocity results in the electron density profile becoming elongated along the path which the streamer has traversed as electrons are required to remain behind the streamer head to neutralize the ions. The space-charge density shows several features. There is a large negative value for n_s close to

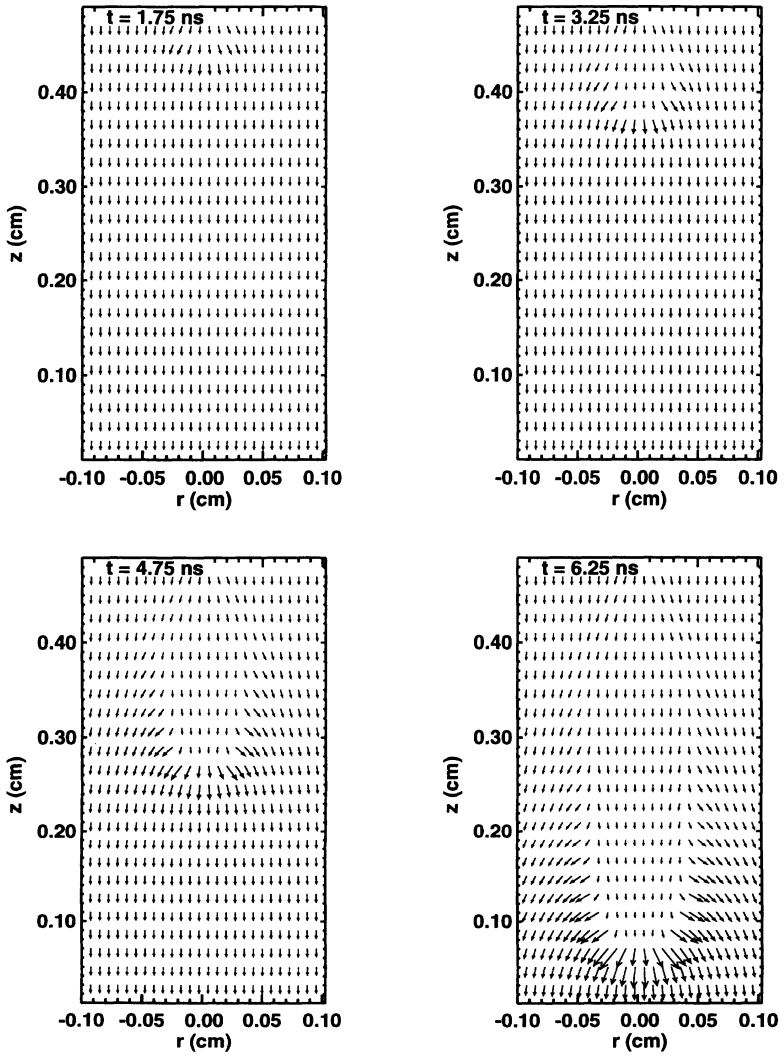

FIG. 5. Velocity flow fields of $\mathbf{v}_T$ at different times for the conditions given in Fig. 1.

the cathode which provides additional electric field shielding for the high plasma density remnant of the initial perturbation. With time the negative space charge becomes increasingly excluded from the high density interior of the streamer and confined to a surface charge about the streamer head. As the streamer passes from the SCP to the FSP positive space charge appears defining the outer radial boundary of the base of the streamer. In the interior of the streamer base, $n_s < 0$, which produces the radial space-charge field necessary to force expansion of the conduction current from the cathode contact point so that it fills the channel. The opening angle of the base is nearly constant implying that the radial expansion velocity of the contact region between the base and the streamer body is roughly constant.

There is a marked evolution in the velocity during the SCP. We show the axial velocity $v_{T_z} - v_{B_z}$ in Fig. 6 instead of simply v_{T_z} so that variations about v_{B_z} can be readily discernible. Note that as the axial velocity v_{T_z} is everywhere negative the positive contours of $v_{T_z} - v_{B_z}$ correspond to $|v_{T_z}| < |v_{B_z}|$. For the conditions considered, $|\mathbf{v}_B| = 1.9 \times 10^7$ cm/s. At $t = 0$ the velocity $\mathbf{v}_T - \mathbf{v}_B$ linearly increases from the center of the high density perturbation and abruptly drops to 0 in the uniform background density. The linear variation comes from the diffusion velocity in the initial Gaussian perturb density profile. As space-charge forces come into play the velocity profile becomes nonlinear. This is due to spatial variations in the density structure (which affect the diffusion velocity) and to the space-charge electric field (which affects the drift velocity). The peak velocity, either radial or axial, increases due to space-charge forces and moves inward to higher densities and shifts towards the streamer head where the space charge is concentrated. Unlike diffusion, which requires a rapid decrease in n_e to generate an appreciable velocity, strong space-

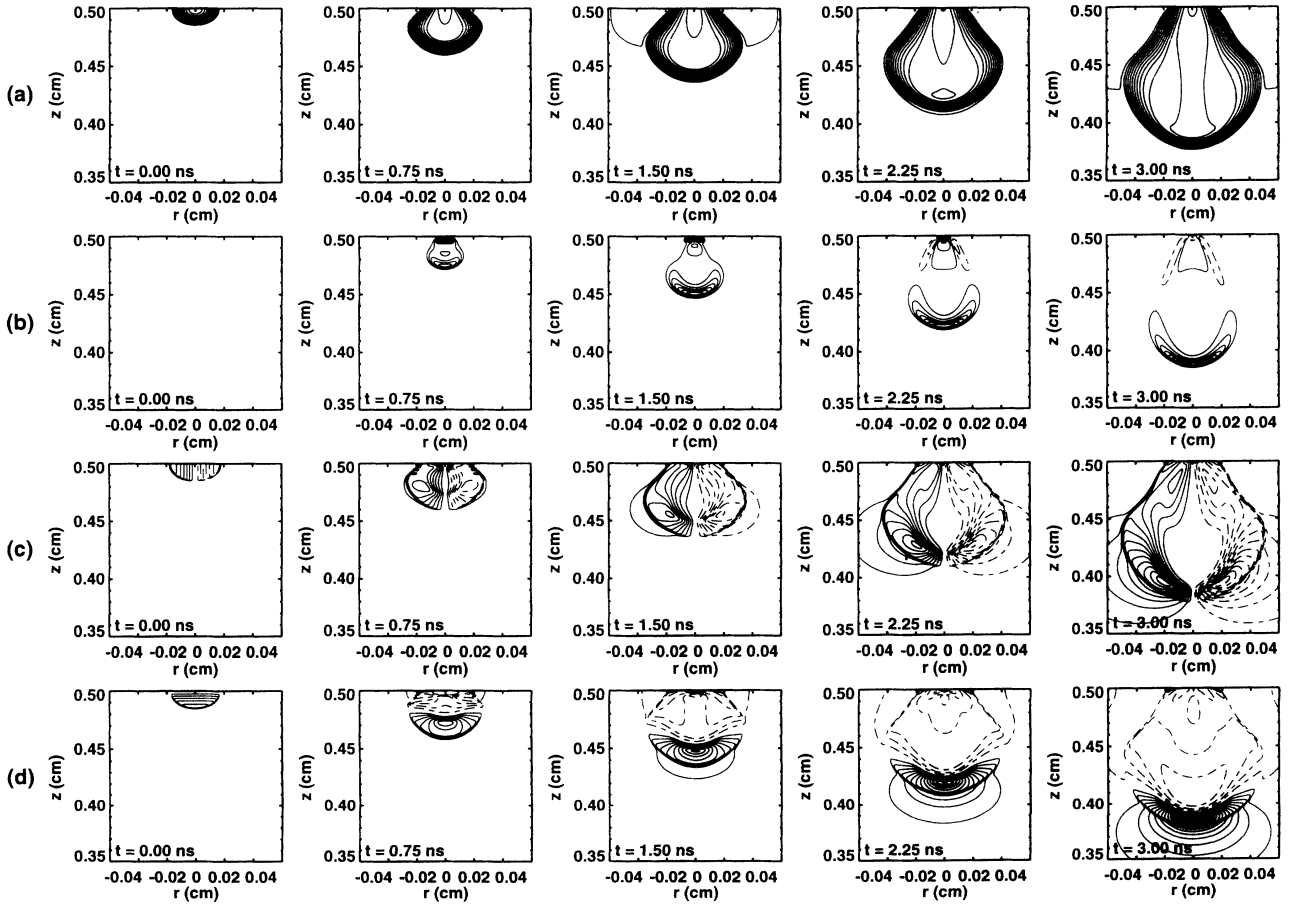

FIG. 6. Contours of $\log_{10} n_e$, n_s, v_{T_r}, and $v_{T_z} - v_{B_z}$ near the cathode for various times during the SCP. The figures of row (a) show the evolution of $\log_{10} n_e$, with the contours spaced by a factor of 10. Row (b) gives the linear profiles of n_s, with solid curves for $n_s < 0$ and dot-dashed contours for $n_s > 0$. A total of ten contours are drawn between the extreme values of n_s. The linear contours of v_{T_r} are shown in row (c), with solid contours for $v_{T_r} < 0$ and dot-dashed contours for $v_{T_r} > 0$. In row (d) are shown the linear contours of $v_{T_z} - v_{B_z}$, with solid contours for $v_{T_z} - v_{B_z} < 0$ and dot-dashed contours for $v_{T_z} - v_{B_z} > 0$. The spacing of the velocity contours is 10^6 cm/s.

charge fields are generated only in regions of relatively high electron density and force the expansion in these regions, generating flatter radial density profiles. The velocity in the streamer body drops with time, with the diffusion velocity decreasing due to the reduced gradients and the drift velocity from space-charge shielding. The space-charge fields also lead to increased velocities in the background plasma exterior to the streamer.

Further details of the SCP evolution are given in the velocity and rate profiles shown in Figs. 7 and 8. The radial profiles for each time are for the value of z for which v_{T_r} has its greatest value. From Fig. 6 we see that this corresponds to a radial slice through the streamer head. The velocity profiles show that with increasing time there is a slight decrease in the peak value of $\mathbf{v}_D$ and a rapid increase in $\mathbf{v}_e$ until $\mathbf{v}_T \simeq \mathbf{v}_e$, except at the outer surface of the streamer where n_e is rapidly decreasing. The peak values of $\mathbf{v}_e$ occur where the shielding space charge is greatest. In the streamer, $\mathbf{v}_D \simeq 0$ where n_e is highest. The space-charge enhanced expansion, which characterizes the SCP, occurs where $\mathbf{v}_T$ increases in the direction of flow. This occurs near the axis for the radial profiles and along the axis in a region through the streamer head roughly to where the shielding space-charge density peaks. Exterior to the volume of expansion, $\mathbf{v}_T$ decreases in the direction of flow leading to a piling up of the electron density, and the formation of the observed precipitous density drop at the boundary of the streamer and the background plasma. Diffusion tends to smooth the front, but is unable to overcome the compression effects of the drift velocity in the space-charge field.

The time evolution of n_e can be described in terms of

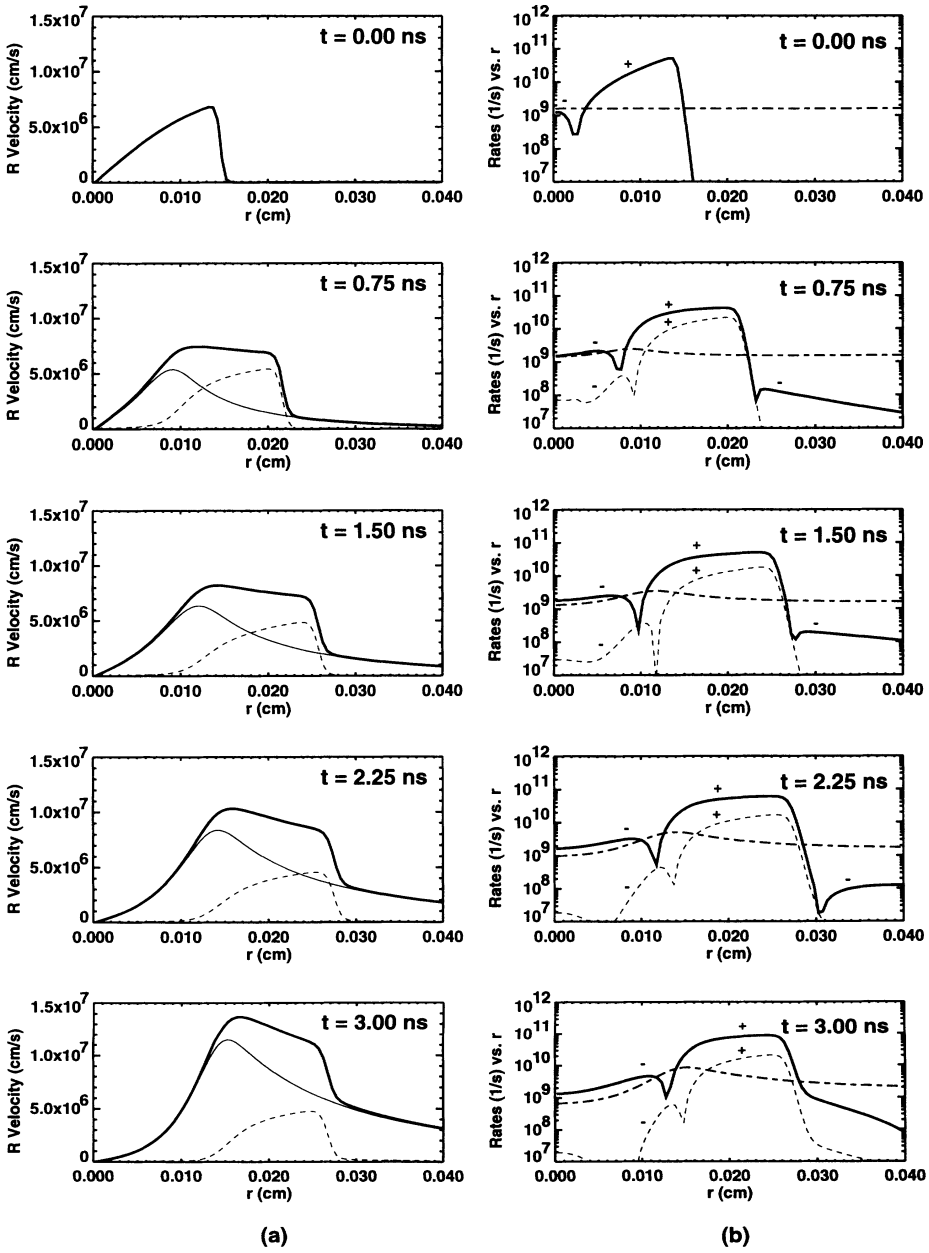

FIG. 7. Radial velocity and rate profiles during the SCP. The figures of column (a) show the radial evolution of v_{T_r} (thick solid curves), v_{e_r} (thin solid curves), and v_{D_r} (dotted curves). The value of z for each radial profile is chosen to be at the position of maximum v_{T_r}. Column (b) gives the radial profiles of the logarithm of $|\omega_T|$ (solid curves), $|\omega_D|$ (dotted curves), and ω_I (dot-dashed curves). The sign of $|\omega_T|$ and $|\omega_D|$ are given above the curves.

three frequencies:

$$\omega_d \equiv -\frac{\nabla \cdot n_e \mathbf{v}_e}{n_e} , \tag{22}$$

$$\omega_D \equiv \frac{\nabla \cdot \mathbf{D}_e \cdot \nabla n_e}{n_e} , \tag{23}$$

$$\omega_I \equiv |\mathbf{v}_e| \alpha , \tag{24}$$

which represent the rate at which n_e changes due to drift velocity, diffusion, and ionization. In Figs. 7 and 8 the absolute magnitude of ω_I, ω_T, and ω_D are shown, where $\omega_T \equiv \omega_d + \omega_D$. The rate ω_T represents the rate of change in n_e due to the total electron velocity. The downward spikes in the curves represent points where the rates change sign. For $t \geq 0$, the diffusion rate is first negative near the axis, then positive near the streamer surface. This rate becomes negligible outside of the streamer in the background plasma. Similarly the total velocity rate is first negative, then positive, and then negative again. Due to the extended space-charge fields, ω_T, while small, remains finite in the background plasma. As the radial profiles are taken through the head of the streamer, where $n_e > n_p$, the flow is not ambipolar and for $t > 0$ we find $|\omega_d| \gg |\omega_D|$. The net effect of radial motion for the electrons is an expansion induced decrease in n_e both close to the axis and at large radii, and an advection-induced compression generated increase in n_e at the surface of the streamer. Along the axis for $t > 0$, ω_T varies from being negative near the cathode where the electron flow diverges to positive in the streamer body where there is a slightly constricting flow. Going from the streamer

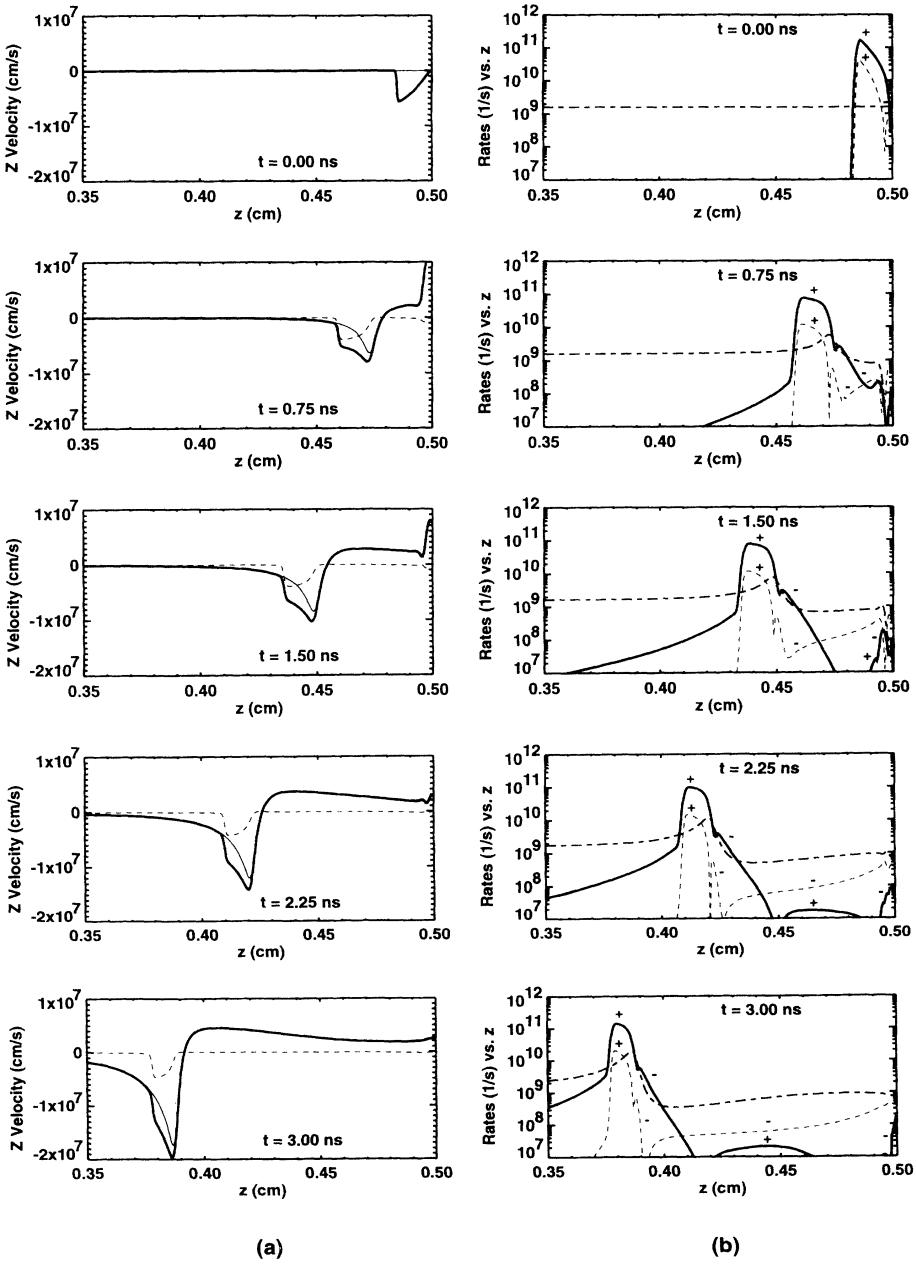

FIG. 8. Axial velocity and rate profiles during the SCP. The figures of column (a) show the axial evolution of $v_{T_z} - v_{B_z}$ (thick solid curves), $v_{e_z} - v_{B_z}$ (thin solid curves), and v_{D_z} (dotted curves). Column (b) gives the axial profiles of the logarithm of $|\omega_T|$ (solid curves), $|\omega_D|$ (dotted curves), and ω_I (dot-dashed curves). The sign of $|\omega_T|$ and $|\omega_D|$ are given above the curves.

body through the streamer head to the background plasma, ω_T becomes negative again and then positive. Because axial flow is less divergent, the total velocity rate along the axis is always positive outside of the streamer unlike its radial behavior, where it is negative at early times. The evolution of the head of the streamer as a separate structure is evident from the axial variation of ω_T. The streamer head can be characterized by the region where ω_T is of high positive magnitude (the outer streamer surface region) combined with the adjacent region of negative ω_T (the inner streamer surface region). The sign change in ω_T across the streamer head reflects how along the axis there is a strong expansion of the electrons at high density which move ahead of the streamer. The streamer body and base are respectively characterized by positive and negative values of ω_T along the axis. Along the axis at the streamer head, $|\omega_d| \gg |\omega_D|$ and $\omega_T \simeq \omega_d$ for $t > 0$. Interior to the streamer the flow is ambipolar with $\omega_D \simeq -\omega_d$ and $|\omega_T| \ll |\omega_d|$. The dynamical change in n_e due to ambipolar flow is very small. In the background electric field (which is greater than the shielded field interior to the streamer body) an ion would move only $\simeq 4$ μm in 2 ns leading to a very small density variation. Changes in n_e interior to the streamer are dominated by the ionization rate ω_I and are not due to dynamical motion.

Even though the ionization rate nowhere achieves values nearly as large as those found for ω_T, ionization is extremely important both through its effect on streamer propagation and on the cumulative growth in the density. A significant feature of ionization is that it strongly compensates for the decrease in n_e caused by space-charge expansion in the inner surface region. The streamer surface has a complex structure. The region where ω_I peaks corresponds roughly to where the shielding space-charge density peaks and where ω_T passes through zero. This surface between the inner and outer surface regions is where ionization produces the electron-ion pairs responsible for the streamer ionization wave propagation. In the outer surface region, ω_T is positive and much greater in magnitude than ω_I. Rapid motion and compression takes place here in the strong space-charge fields and it is

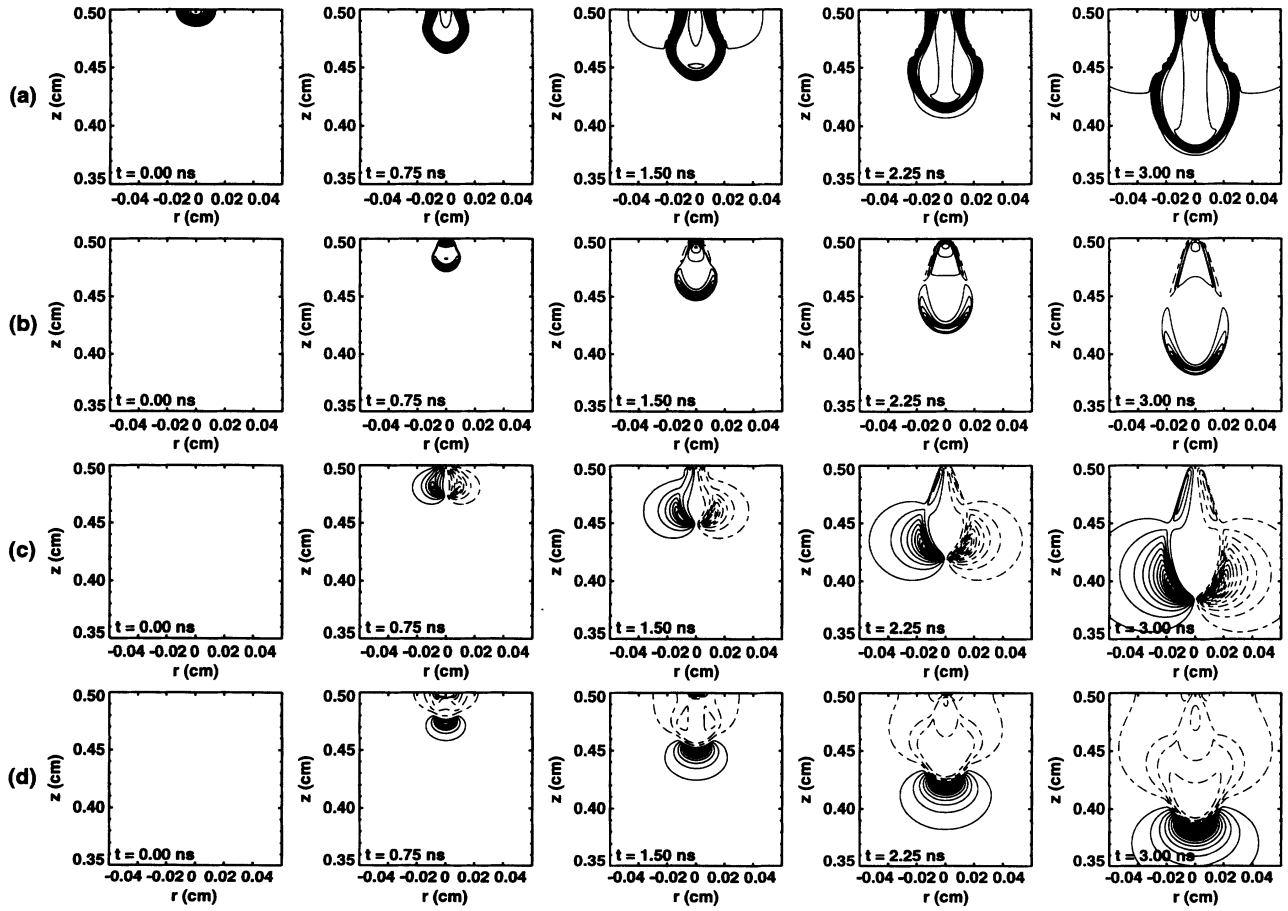

FIG. 9. Streamer evolution during the SCP neglecting the effects of diffusion. The figures of row (a) show the evolution of $\log_{10} n_e$ with the contours spaced by a factor of 10. Row (b) gives the linear profiles of n_s, with solid curves for $n_s < 0$ and dot-dashed contours for $n_s > 0$. A total of ten contours are drawn between the extreme values of n_s. The linear contours of v_{T_r} are shown in row (c), with solid contours for $v_{T_r} < 0$ and dot-dashed contours for $v_{T_r} > 0$. In row (d) is shown the linear contours of $v_{T_z} - v_{B_z}$, with solid contours for $v_{T_z} - v_{B_z} < 0$ and dot-dashed contours for $v_{T_z} - v_{B_z} > 0$. The spacing of the velocity contours is 10^6 cm/s.

in this region that has by far the shortest time scale. As noted before, the strong compression is the cause for the sharp density profile at the streamer surface. The short ω_T time scale in the outer surface does not appear to dominate the streamer evolution as the electron density is very low throughout this region. As the joining of the streamer to the background takes place at a distance from where ionization is producing the electrons, the negative streamer ionization wave can propagate independently of low density background plasma altogether. Further ahead of the streamer surface, where ionization again is the fastest process, an extended region of enhanced ionization develops as the space-charge field strengthens with time.

To determine how significant diffusion is in the SCP we have studied streamer evolution without diffusion ($\mathbf{D}_e = 0$) using the same initial conditions. Results are shown in Fig. 9. Qualitatively there is little difference with and without diffusion. The radial profiles are definitely narrower without diffusion, and higher electron densities and velocities are found, with the shielding space charge being confined to a thinner surface layer. The drop off in n_e about the streamer head, body, and base is more rapid. This behavior is expected with no mitigating diffusion to broaden the streamer surface. Space-charge expansion does dominate in the SCP for our calculations, but diffusion should not be neglected in general as it may play a significant role for other discharge parameters.

C. Filamentary streamer phase

During the FSP the discharge develops the filamentary structure characteristic of streamers. The 2D evolution of the electron density and the space-charge density are shown in the contour plots in Fig. 10. The separation of the streamer from the background plasma occurs at a very sharp surface where space-charge shielding takes place. Although the space-charge contours show that n_s is strongly peaked at the tip of the streamer head there is considerable space charge along the surface along the side of the streamer body. From the space-charge per unit axial length $2\pi \int_0^\infty n_s r\, dr$, which is plotted in Fig. 11 for $t = 6.25$ ns, we see that the bulk of the space charge in

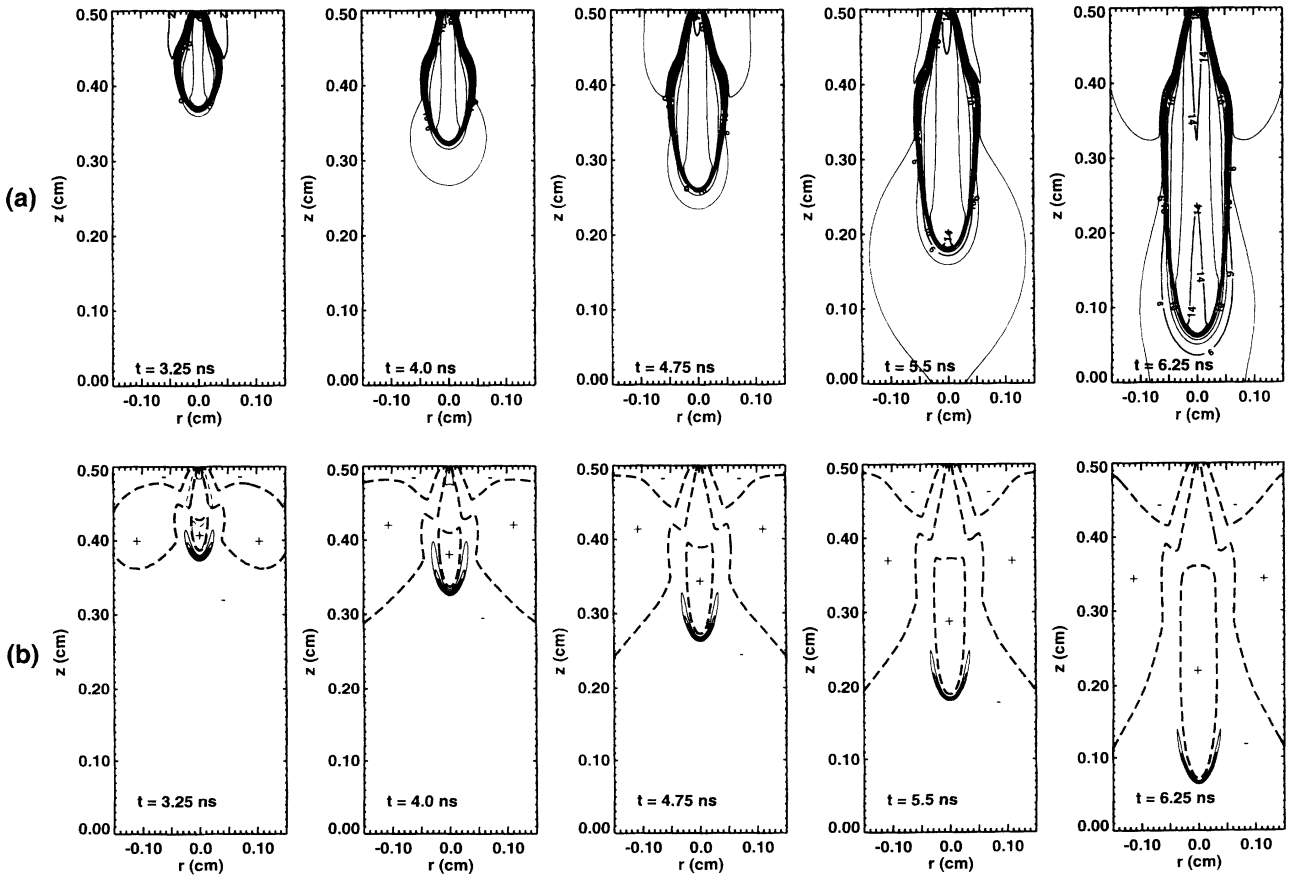

FIG. 10. Contours showing the evolution during the FSP of (a) the logarithm of the electron density and (b) the linear space-charge density. The contours of n_e are separated by a factor of 10 in density. For n_s, ten contours running from the most negative to the most positive value are shown at each time step. Space-charge contours for $n_s > 0$ are shown as dashed curves, while those for $n_s < 0$ are given as thin solid curves. The thick dashed curves correspond to $n_s = 0$ and bound regions where a + or a − designates the sign of the space charge.

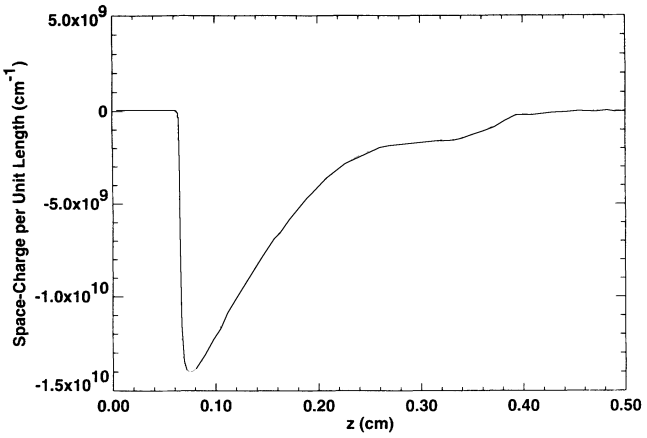

FIG. 11. Space-charge per unit axial length during the FSP. This profile corresponds to the contours of n_s given in Fig. 10 at $t=6.25$ ns.

the streamer at late times is not associated with the tip of the streamer head, but with the shielding about streamer head and body. The base region of the streamer is also distinguished by having nearly zero space-charge per unit axial length.

Along the surface of the streamer body there is continued radial expansion of the streamer surface during the FSP (see Fig. 10). This expansion is evident at each fixed axial point and is greatest close to the streamer head. At a fixed axial position in the streamer base there is little radial expansion of the streamer surface. The boundary of the base region expands axially, away from the cathode, at roughly the background field drift velocity and radially so as to match onto the streamer body. The constant opening angle of the base regime implies a constant radial expansion velocity of the region where the base joins with the streamer body. The radius of the matching point grows linearly with time with a velocity that is roughly $\frac{1}{3}|\mathbf{v}_B|$, and its axial position moves at nearly $|\mathbf{v}_B|$. As the streamer propagation velocity increases roughly exponentially with time, the width of the streamer therefore varies as the logarithm of the streamer length.

To clarify details of the streamer filament structure, we show in Fig. 12 three-dimensional surface plots of the densities and field magnitude. The electron density profile shows that there is a distinctive enhancement in n_e at the head of the streamer which folds about the body of the streamer, disappearing where the streamer narrows at the base. This enhancement in n_e corresponds to the surface shielding space charge, as is shown in Fig. 12(b). The peak in n_e at the streamer base is a reflection of the initial high density perturbation at the cathode. Because of the large variation in n_e, which is typical in streamers, it is misleading to simply consider linear profiles of n_e. Additional structure in the streamer electron density profile is observed in Fig. 12(c), which gives the profile of the logarithm of the electron density. The region where there is a rapid drop off in n_e corresponds to the outer surface region of the streamer where shielding takes place. Exterior to this region the Debye length becomes larger than any other length scale and the plasma is no longer quasineutral. The depression in the logarithm of the electron density exterior to the base of the streamer shows a region outside of the streamer where there is a local minimum in $|E|$. The lower electric field results in a less rapid growth via collisional ionization of the initially uniform background density than far away from the streamer. The region of increased preionization density about the streamer head, caused by the rapid ionization in the streamer head space-charge field, extends over a large volume about the streamer.

The profile of $|E|$, shown in Fig. 12(d), exhibits this enhanced field, as well as the reduced shielded field interior to the streamer. In the streamer body there is little radial variation of $|E|$ near the axis. Along the side of the streamer body at the surface, $|E|$ shows a slight drop just before abruptly rising to either the enhance field near the streamer head or the background field far behind the streamer head. Even though the electron density in the body of the streamer is sufficiently high so that one might expect complete shielding of the electric field (i.e., the Debye length is much shorter than the streamer radius and the dielectronic relaxation time scale is also shorter than the streamer propagation time), current conservation requires that there be a finite (and in this case significant) interior electric field which drives the electron conduction current through the streamer body. The induction current can be approximated as $I_i \simeq \epsilon_o \pi R_h^2 E_h v_s / R_h$, where E_h is the peak electric field magnitude at the streamer head and R_h is the corresponding radius of curvature of the space-charge shielding at the streamer head. Equating this to the conduction current in the streamer body $I_c \simeq e\pi r_e^2 n_{e_b} \mu_e E_b$, we find the electric field magnitude in the streamer body to be

$$E_b \simeq \frac{R_h E_h v_s \epsilon_0}{r_e^2 n_{e_b} e \mu_e} , \tag{25}$$

with n_{e_b} being the electron density at the point at which E_b is evaluated, and r_e being the radius at which the density drops to $1/e$ of its axial value. This relation was found to agree well with our numerical results.

On several points of streamer evolution we find agreement with the perfectly conducting model [52] of the streamer filament. The streamer head and body in our simulations are quite similar to an ellipsoid of revolution, and the radius of curvature of the streamer head is nearly constant in time in the FSP. The screening surface however is not an equipotential surface as would be the case for a perfectly conducting plasma. This is clearly evident from the axial field profiles in Fig. 2 and from the flowfields shown in Fig. 5. We find that interior to the streamer at the base and over much of the body of the streamer the potential differs only slightly from the background value at the same axial position. It is only near the streamer head that there is a strong modification in the potential.

The shape of the streamer surface in the FSP is dynamically determined by the space-charge dominated forces governing the electron velocity. Contours of the velocity

during the FSP are given in Fig. 13. There is a rapid temporal growth of the magnitude of the velocity which occurs exclusively in the region external to the streamer. The 2D nature of the streamer head development is visible in this figure. High values of the axial velocity are localized close to the tip of the streamer head. This implies that dominantly axial motion of the streamer ionization wave is also a localized phenomenon confined to small radii. Looking back from the tip of the streamer head, we see that the radial velocity remains high over an extended region of the surface. The streamer propagation can thus be described as z displacement close to the axis followed by a rapid radial expansion.

The propagation of the streamer does not simply involve an axial displacement of the streamer plasma. Throughout the FSP there is a continuance of the dominance of $\mathbf{v}_e$ over $\mathbf{v}_D$ (see Fig. 14). This is primarily due to the growth of $\mathbf{v}_e$. The maximum diffusion velocities are somewhat underestimated as they are limited in magnitude to $v_{D_r} \lesssim 2D_{e_{rr}}/\Delta r$ and $v_{D_z} \lesssim 2D_{e_{zz}}/\Delta z$ by the finite spatial resolution. For our 5-μm resolution, this implies that $v_{D_r} \lesssim 8\times 10^6$ cm/s and $v_{D_z} \lesssim 7\times 10^6$ cm/s. As $\mathbf{v}_e$ increases with time at the streamer head, the ratio of the maximum axial and radial components of $\mathbf{v}_e$ remains nearly constant in time.

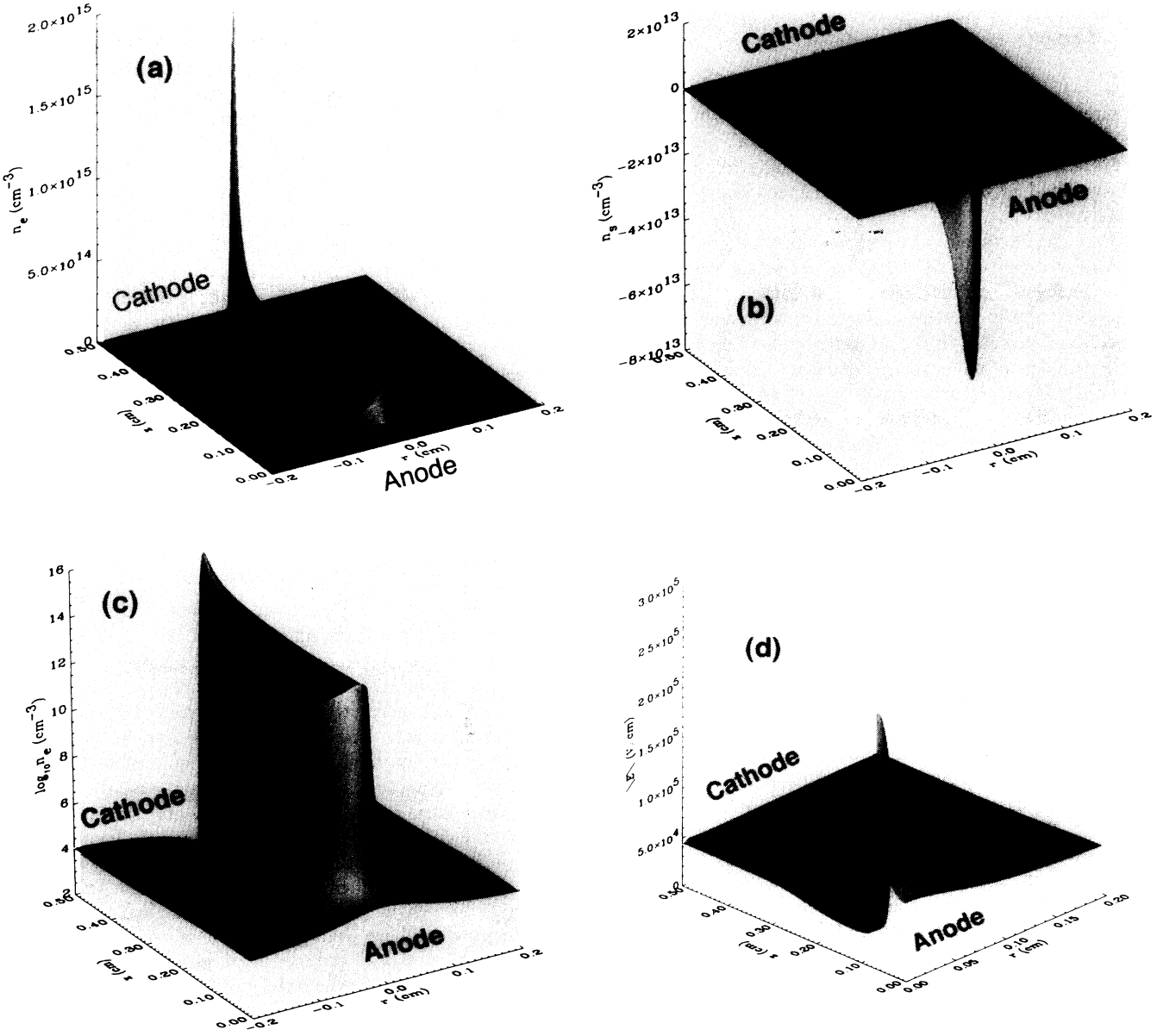

FIG. 12. Details of the filamentary structure for a typical negative streamer during the FSP. The figures show (a) the electron density profile, (b) the space-charge density profile, (c) the logarithm of the electron density profile, and (d) the profile of $|E|$. The profiles correspond to contours given in Fig. 10 at $t = 6.25$ ns.

To study how the radial structure evolves during the FSP we consider next the time history of the velocity and density profiles at a fixed axial point of $z=0.4$ cm (see Fig. 15). The head of the streamer reaches $z=0.4$ cm at $t\simeq 2.75$ ns for the conditions considered. Radial motion is dominated by the space-charge generated drift velocity. Near the axis, v_{e_r} changes from being outward to inward directed as the streamer head passes. The inward radial motion occurs in the high density quasineutral regime where $\nabla\cdot n_e \mathbf{v}_T \simeq 0$ and does not lead to a significant change in the electron density. Outward expansion however takes place at and beyond the shielding layer where the electrons are not bound to ions. This results in the extension with time of the shielding surface to larger radii. This is not simply a free expansion of the shielding electrons, as this would lead to the removal of the shielding layer entirely. As the shielding electrons move outward, continued ionization takes place leaving behind ions which are nearly stationary on the time scales of interest here. These ions are then neutralized by electrons flowing from the streamer interior, leaving a quasineutral plasma behind as the shielding layer moves.

This radial expansion continues until $t\simeq 4.5$ ns, at which time the axial extension of the streamer base reaches $z=0.4$ cm (see Figs. 1 and 10). At this time the sign of the space charge reverses, both interior to the streamer and at the surface. This results in the radial electron drift velocity becoming positive at all radii. Radial expansion of the shielding surface slows and then stops by $t\simeq 6.5$ ns. Electrons flow within the now nonmoving streamer surface in the base region with $\nabla\cdot n_e \mathbf{v}_T \simeq 0$. Increases in n_e occur primarily due to ionization at a rate similar to that in the background field.

A streamer has a complex radial structure which can not be adequately described by a single length scale. We make use of two radial length scales. The e-folding radius r_e was previously defined and represents the interior electron density length scale at the axis. The shielding radius r_s, corresponds to the boundary between the streamer plasma and the background plasma where strong space-charge shielding takes place and represents the large scale structure of the streamer. Except at the tip of the streamer head and close to the cathode, $r_s \gg r_e$. Figure 16 shows the axial variation of r_e and r_s during the FSP just prior to the streamer reaching the anode. As the thickness of the shielding space-charge layer varies with axial position, we describe r_s by plotting the contours evaluated at the 90% level of the maximum of $|n_s|$ at each radius. For comparison, this figure shows results for streamer evolution neglecting diffusion. The e-folding radius rapidly increases with distance from the cathode at the streamer base. Along the body of the

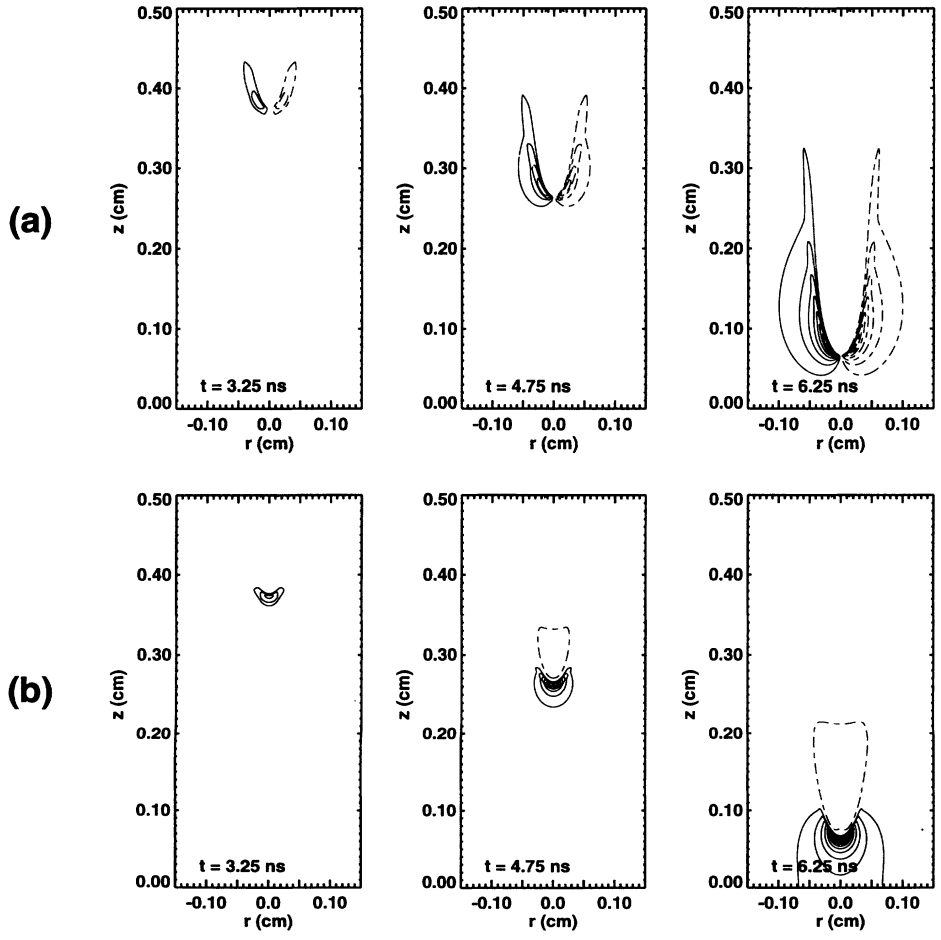

FIG. 13. Contours of v_{T_r} and of $v_{T_z}-v_{B_z}$ for various times during the FSP. The figures of row (a) show the linear contours of v_{T_r} with solid contours for $v_{T_r}<0$ and dot-dashed contours for $v_{T_r}>0$. In row (b) is shown the linear contours of $v_{T_z}-v_{B_z}$, with solid contours for $v_{T_z}-v_{B_z}<0$ and dot-dashed contours for $v_{T_z}-v_{B_z}>0$. The spacing of the velocity contours is 6×10^6 cm/s.

streamer there is a slow increase in r_e, with the mean radius being roughly 160 μm with diffusion and 120 μm without diffusion. The decrease in r_e close to the anode (which occurs earlier if diffusion is neglected) is due to the increased streamer head space-charge field from mirror charges at the anode. The width of the shielding layer increases away from the streamer head, and narrows again at the base of the streamer. Estimates of the streamer head electric field must be based upon the radius of curvature evaluated from r_s and not r_e. Neglecting diffusion leads to smaller values for both r_e and r_s. The base expansion rates with and without diffusion are nearly identical showing that space-charge forces determine the streamer radial structure.

Very little modeling of the nonlinear radial structure of streamers has been done. A simple analytic model of the radial expansion in the SCP, including space-charge effects, was developed by Babich [22]. This model treated streamer evolution from the AP through the SCP to the beginning of the FSP. Babich predicted that the radial electron density profile would expand exponentially in the SCP when the electron drift velocity due to space charge became larger than the diffusion velocity. This rapid expansion would then continue until the radius $1/(2\alpha_B)$ was reached, with α_B being the ionization rate in the background field. Further expansion was predicted to take place on the very slow ambipolar time scale. Our results do not show evidence of exponential expansion during the SCP. The expansion observed during the SCP was found to be roughly linear with time. Also the expansion did not stop at $1/(2\alpha_B)$, which was $\simeq 60$ μm, but continued on until $r_e \simeq 160$ μm, which corresponds to $1/(2\alpha)$ for $E \simeq 40\,000$ V/cm and not the background value of 50 000 V/cm. The shielding radius, which is more tightly coupled to the space-charge fields than is r_e, gave an even poorer fit to the predicted streamer radius and continued to expand after the SCP at a rate well above that due to ambipolar motion. Simulations which we have performed for E_B between 40 000–80 000 V/cm show little variation in the final value of r_e. One must be careful in assuming that because, in the interior of the streamer, n_e becomes large and the Debye length short the surface expansion must be ambipolar. As we have shown, this is not the case for streamers.

Streamers propagate through a nonlinear ionization wave. The details of this ionization wave propagation mechanism are poorly understood. At the surface of the streamer head there is a strong interaction between ionization and electron motion in the space-charge field, which combine to produce the ionization wave propagation. To show the variation of the relevant time scales affecting streamer propagation during the FSP we plot in

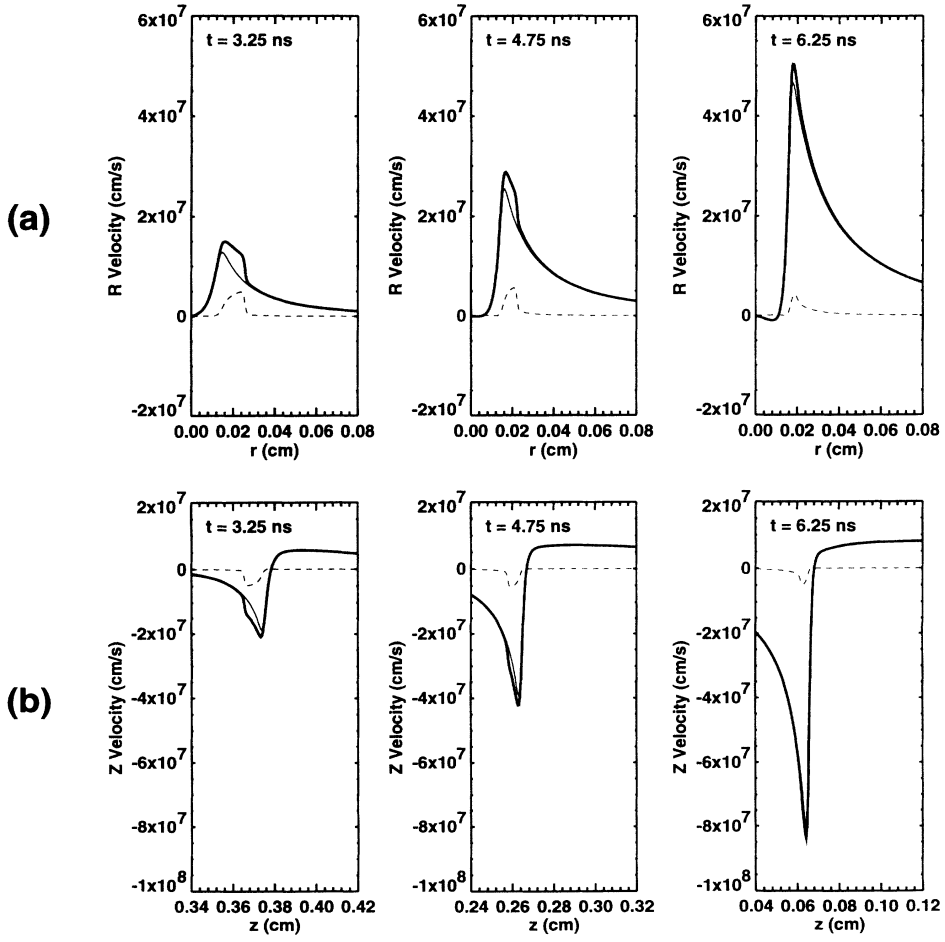

FIG. 14. Radial and axial velocity profiles about the streamer head during the FSP. The figures of row (a) show the radial evolution of v_{T_r} (thick solid curves), v_{e_r} (thin solid curves), and v_{D_r} (dotted curves). The value of z for each radial profile is chosen to be at the position of maximum v_{T_r}. The figures in row (b) show the axial evolution of $v_{T_z} - v_{B_z}$ (thick solid curves), $v_{e_z} - v_{B_z}$ (thin solid curves), and v_{D_r} (dotted curves).

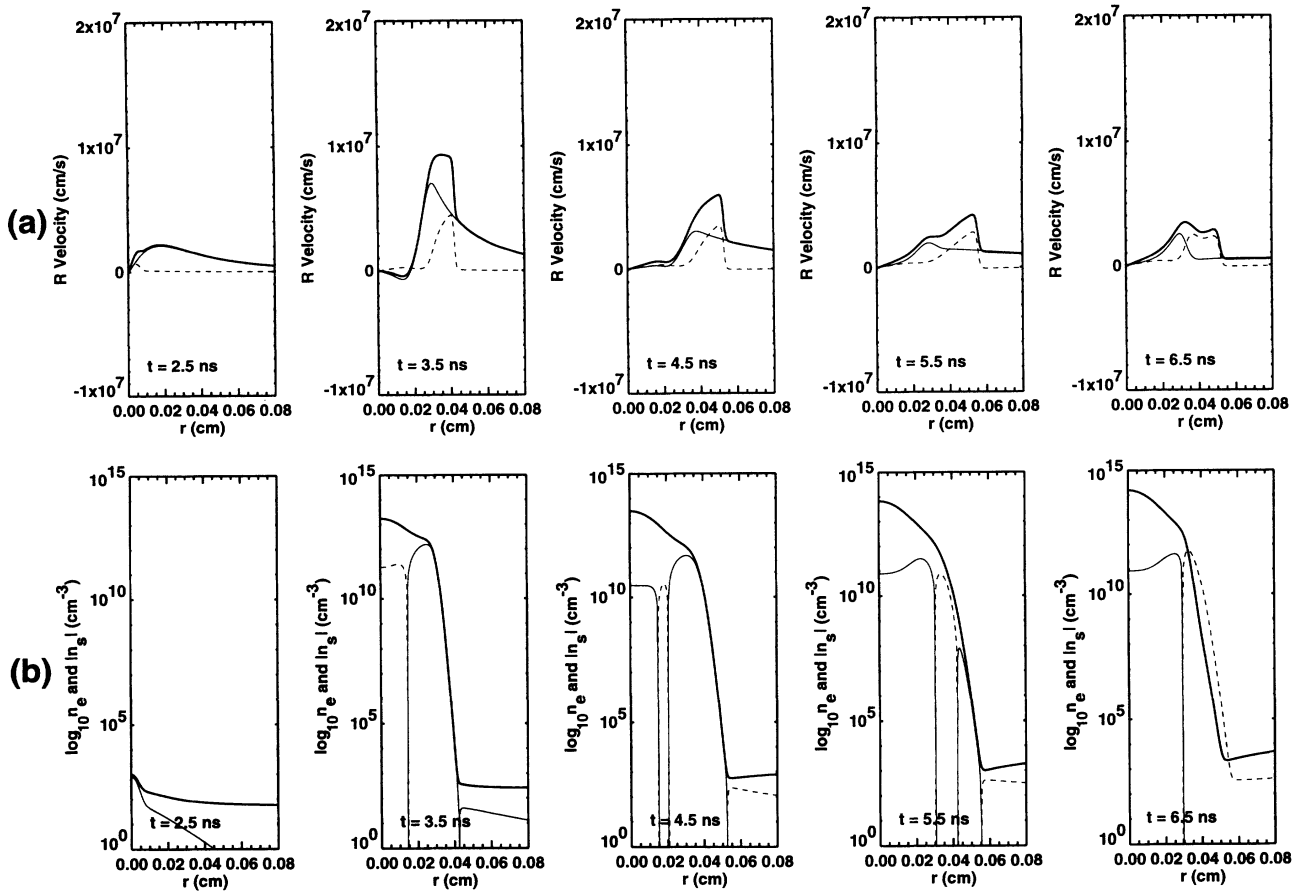

FIG. 15. Streamer evolution at a fixed axial position of $z=0.4$ cm. Figures in row (a) show profiles of v_{T_r} (thick solid curves), v_{e_r} (thin solid curves), and v_{D_r} (dotted curves), while those in row (b) give profiles of n_e (thick solid curves), $n_s<0$ (thin solid curves), and $n_s>0$ (dotted curves).

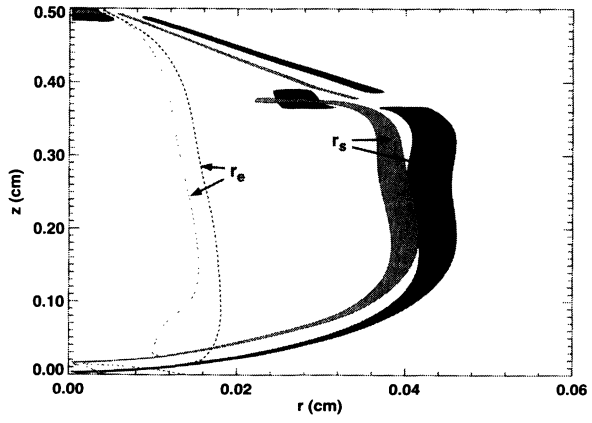

FIG. 16. Profiles of r_e (dotted curves) and r_s (solid contours). The shielding radius is represented by contours at the 90% level of the maximum of $|n_s|$ at each axial point. The thick curve and dark shaded region represent a model simulation including diffusion for $t=6.5$ ns. The thin curve and light shaded region show results neglecting diffusion at $t=6.25$ ns.

Fig. 17 the axial variation of the relevant rates. Except in the streamer interior, the diffusion rate is much slower than that due to the drift velocity. In the body of the streamer, $\omega_d \simeq -\omega_D$ and $\omega_I \gg |\omega_d| \gg |\omega_d+\omega_D|$, with the resulting flow being ambipolar. The ionization rate also dominates ahead of the streamer due to the extended space-charge electric field. The drift velocity rate is the largest rate only in a thin region at the head of the streamer.

It is difficult to see in Fig. 17, because of the narrowness of this layer, that $|\omega_d| \gg \omega_I$ in two zones, as was the case in the SCP. Between these zones, ω_d goes through zero and the ionization rate dominates. Rapid variations in the rates at the streamer head take place just where there is a rapid jump in n_e. To view the effect of the rates in changing the density in a region about the streamer head we plot rates weighted by n_e, which gives their true contributions to $\dot{n}_e$. This is shown in Fig. 18, where n_e and n_s are also given. The inner surface region where $\omega_T<0$ and $|\omega_T|>\omega_I$ and the outer region where $\omega_T>0$ and $|\omega_T|>\omega_I$ are equally important.

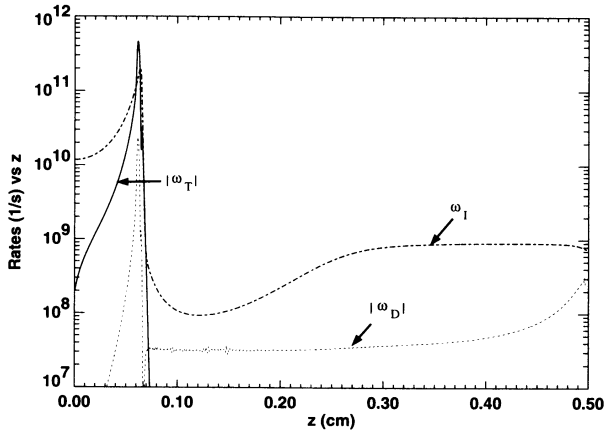

FIG. 17. Axial profiles of the electron continuity equation rates at $t=6.25$ ns.

The combined regions where ω_T dominates ω_I determine the dynamic change in the shielding electron density with streamer propagation. Where $\omega_T<0$ and $|\omega_T|>\omega_I$, the electron density is decreasing with time. This represents the expulsion of the shielding electrons at the streamer head. Electrons are rapidly pushed ahead of the streamer in the region where $\omega_T>0$ and $|\omega_T|>\omega_I$.

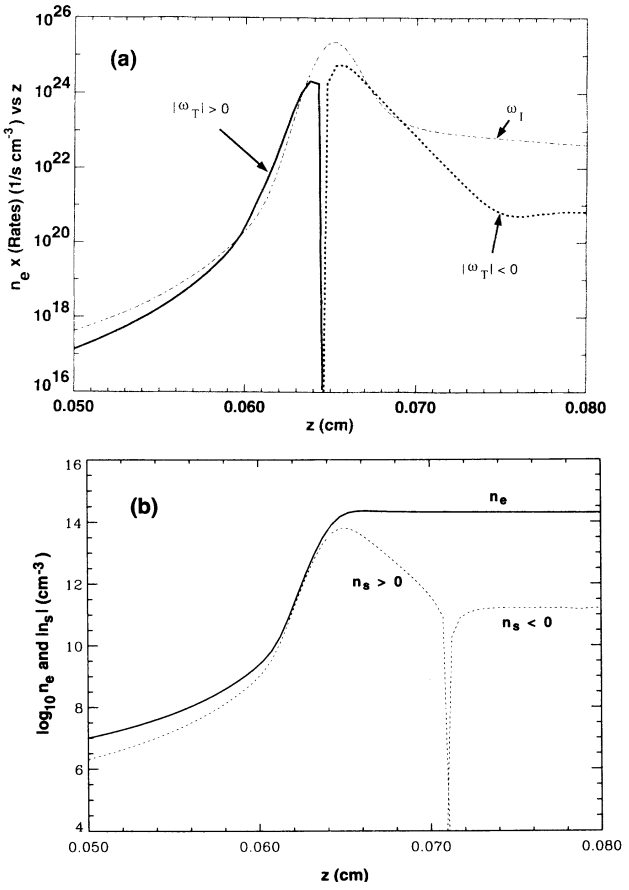

FIG. 18. Axial profiles at the streamer head in the FSP at $t=6.25$ ns of (a) the electron continuity equation rates ω_T and ω_I weighted by n_e and (b) the logarithm of n_e and $|n_s|$.

The separation of the streamer from the background corresponds to the point in front of the streamer head where ω_T becomes less than ω_I so that dynamic effects become less important in modifying the electron density than the preionization enhancement. If there were no ionization and charge neutrality were not required in the streamer body, then the dynamic changes in n_e would correspond to the simple motion of the electrons in streamer head. Because of the large ion density in the streamer body, ionization is needed to create new electron-ion pairs or the streamer propagation would slow to the ambipolar time scale. Ionization is responsible for the streamer propagation being faster than the electron drift or even combined drift and diffusion velocities. The thickness of the region where maximum ionization takes place is $\simeq 20$ μm. Over this region ionization increases the electron density several orders of magnitude and the space-charge density is maximum. The jump in the density however is not sufficient to bring the background density up to the density in the body of the streamer. The total jump in density requires the combined action of advection and compression to work with the ionization enhancement.

The rate analysis by Wang and Kunhardt [41] for 2D streamers modeled with low spatial resolution shows similar behavior to that described here. Due to their course grid spacing the detailed time-scale variations at the streamer head are not evident in their study. Their modeling also concludes that n_e is nearly constant in space within the streamer body. We find with higher resolution that large spatial variations of n_e within the streamer are prevalent.

D. Streamer dependence on n_G and r_G and on the cathode boundary condition

The initial conditions considered in our modeling bypass the avalanche phase of streamer development and assume current continuity at the cathode. We consider here the sensitivity of our results to these initial conditions and to the current boundary condition. For comparison we also present results for the FSP of a simulation without diffusion. We first show in Fig. 19 the evolution of n_e without diffusion with $n_G=10^{14}$ cm^{-3} as before, and with diffusion for a smaller initial Gaussian perturbation density $n_G=10^{12}$ cm^{-3}. These logarithmic contours show the large scale streamer structure, such as the position of the shielding surface. Comparing these profiles with those given in Fig. 10 it is clear that the primary effect of decreasing the perturbation density is in delaying the development of FSP. Contours for $n_G=10^{14}$ cm^{-3} at $t=6.25$ ns and for $n_G=10^{12}$ cm^{-3} at $t=7.75$ ns are nearly identical at the streamer head and body. For the lower initial density the streamer tail region is longer due to the longer time spent in the SCP. The logarithmic density profiles with $n_G=10^{14}$ cm^{-3}, but with diffusion neglected, are slightly narrower at the streamer head and appreciably narrower at the base and where the base region joins the streamer body. The density is also higher along the axis in the streamer body. The case without diffusion also evolves slightly faster than when diffusion is included. The effects of diffusion here are not very

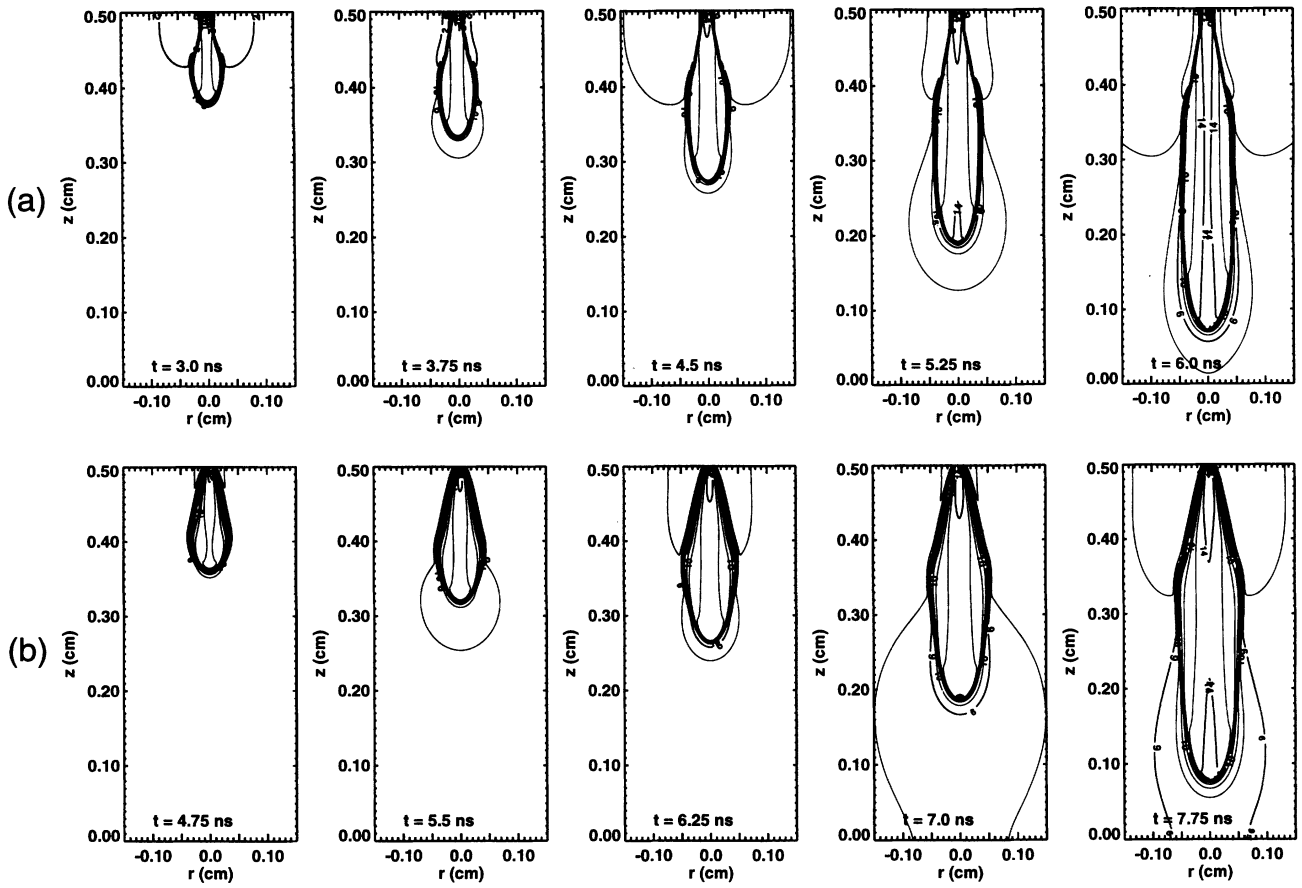

FIG. 19. Effects on streamer evolution due to the neglect of diffusion and of a lower value of n_G. Initial conditions used were the plane-parallel gap with separation 0.5 cm, fixed voltage 25 kV, $n_B = 1$ cm^{-3}, and $r_G = 25$ μm. The figures in row (a) are for $n_G = 10^{14}$ cm^{-3} and no diffusion. In row (b) the perturbation density is $n_G = 10^{12}$ cm^{-3} and diffusion is included. The contours show the evolution during the FSP of the logarithm of the electron density. Contours are separated by a factor of 10 in density.

significant, but may be for other streamer parameters. Variations in the initial perturbation radius were also found to have weak effects on the streamer structure in the FSP. Figure 20 gives the logarithmic density profile evolution for $r_G = 100$ μm and $r_G = 200$ μm. While there are large variations in the density profiles at the streamer base, the structure of the streamer body and head again evolve to nearly identical profiles by the time the streamer crosses the gap. With increasing r_G the streamer spends less time in the SCP, with the resulting streamer crossing time diminishing.

To test the sensitivity of the negative streamer development on our continuous current boundary condition we consider the streamer evolution where we have moved the cathode from $z = 0.5$ to 0.6 cm, while keeping the background electric field the same as before and with the Gaussian perturbation again placed at $z = 0.5$ cm. The gap voltage used was 30 kV. A double headed streamer develops, with the negative streamer as before propagating towards the anode, and a positive streamer now forming at late times on the cathode side of a filament. Contours of the electron and space-charge density are shown in Fig. 21. The space-charge contours about the streamer head differ considerably from those in Fig. 10 because the extreme concentration of positive charge which builds up at the positive streamer head distorts the contour spacing. For the double headed streamer case the base region is very narrow, with high positive space charge being concentrated about the $z = 0.5$ initial perturbation position until $t \simeq 8$ ns. After this time the positive streamer shows rapid motion towards the cathode. A very low initial background density ($n_B = 10^{-5}$ cm^{-3}) was used to prevent the development of the positive streamer until after the negative streamer reached the anode. If $n_B = 1$ cm^{-3} were used, as was the case for the other calculations presented, the positive streamer would form earlier. We find that for this test problem, low initial background densities ($n_B \lesssim 10^5$ cm^{-3}) lead to positive streamers with extremely high fields with corresponding short length scales that cannot be resolved adequately with the 5-μm grid which we use. Positive streamer evolution can therefore only be followed for a short interval in time under this condition. There are no qualitative differences between the negative streamer which forms adjacent to a positive streamer head and the single headed negative streamers. We do see that the evolution is slower, and has lower density than the corresponding single streamer case. These differences may be due to the fact that the double headed space-charge field for the negative streamer is smaller (with correspondingly smaller ionization

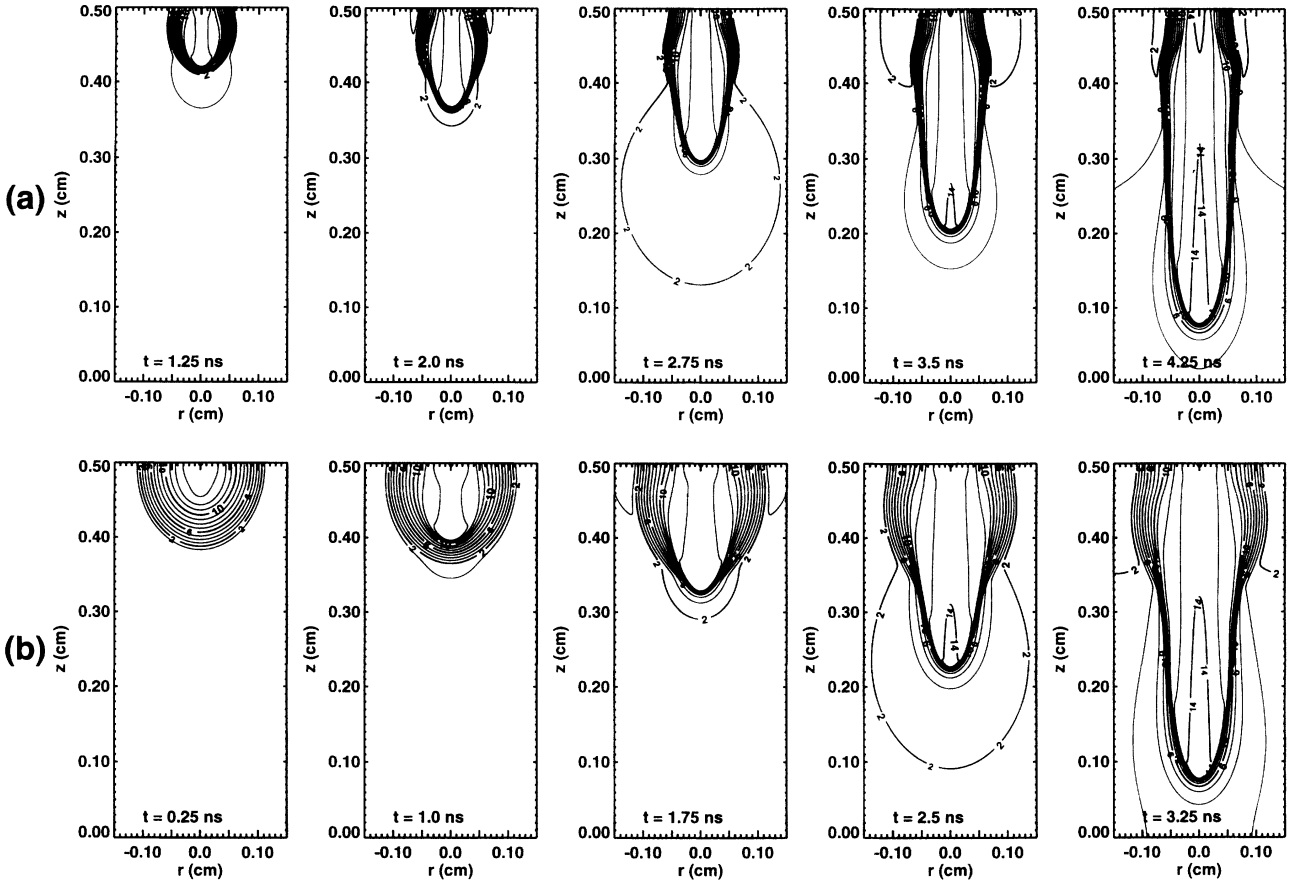

FIG. 20. Effects on streamer evolution during the FSP due to variations in r_G. The figures show the contours of the logarithm of the electron density separated by a factor of 10 in density. For the figures in row (a) the initial perturbation size was $r_G = 100$ μm, while for those in row (b) the initial perturbation size was $r_G = 200$ μm.

rates and electron drift velocities). This is because less negative space-charge density is needed to produce similar shielded internal electric fields when the positive space charge is nearly fixed in space than when the positive space charge corresponds to moving mirror charges beyond the cathode. There is a consistent pattern of behavior evident in all the cases presented, which shows that slower negative streamer development leads to lower electron densities, streamer propagation velocities, and peak electric fields.

We have seen that in the FSP the large scale structure, such as the shielding radius, is weakly dependent upon the initial perturbation and boundary conditions. This holds as well for the shorter scale structure typified by the e-folding radius. The time evolution of r_e for the cases considered above are shown in Fig. 22. In front of the streamer head, r_e becomes infinite in the background plasma, which has less than a factor of e radial variation. The local peak in r_e at the streamer head is due to the electron density about the head which is responsible for space-charge shielding. The SCP evolution of r_e is very dependant on initial conditions. For $r_G = 25$ and 100 μm [Figs. 22(a) and 22(b)], r_e increases nearly monotonically with streamer length, with rapid increases in the SCP followed by a slow increase in the FSP. For $r_G = 200$ μm [Fig. 22(c)], r_e overshoots in the SCP and then decreases back to the FSP value. After the passing of the streamer front, r_e is nearly constant in time at each axial position. There is a slow decrease with time of r_e at $z \simeq 0.45$ cm for the 100 and 200 μm cases. This is not due to an inward radial motion of the plasma because the plasma there is quasineutral and the ion motion is too slow to allow appreciable density variations on the time scales considered. The variation in r_e instead comes from enhanced ionization close to the axis which leads to a narrowing of the radial density profile. For the larger initial radii simulations, the shielded electric field magnitude near the streamer base develops a local maximum on axis which results in increased ionization and the effective decrease in r_e. We note that aside from this effect there is no evidence from variations in r_e of the axial motion of the base region which is clearly evident in the logarithmic contour plots of n_e for all values of r_G. This emphasizes the necessity for considering more than simply the e-folding radius in studying streamer morphology. The evolution of r_e for $n_G = 10^{12}$ cm^{-3}, for the case without diffusion, and for the double headed streamer case are shown re-

spectively in Figs. 22(d), 22(e), and 22(f). There is remarkable little variance in the value of r_e along the streamer body in the FSP for all six cases shown. This implies that in the FSP the small scale structures, like the large scale structures, are insensitive to how the streamer forms.

In the modeling by Dhali and Williams [38] it was found that the streamer radius was strongly dependent on (and in fact roughly equal to) the initial radial scale of the density perturbation. The primary difference in their calculations, other than lower resolution, was the use of a much higher uniform initial preionization density which typically was 10^8 cm^{-3} rather than the 1 cm^{-3} values used in this paper. From our simulations we have found that high preionization densities can lead to the streamer passing from the FSP to a second expansion phase (the ESP) which differs from the SCP [15]. The conditions treated by Dhali and Williams result in streamers that pass through multiple phases of radial variation, making it difficult to predict the overall radial dependence.

While the overall streamer structure shows a weak dependence of the FSP structure on initial conditions, a more careful analysis shows that there are significant initial condition effects. From the spacing of the streamer head positions in Fig. 22 it is evident that there is a large variation in the streamer propagation speed in FSP for the several cases considered. Profiles of v_s as a function of the streamer head position plotted in Fig. 23 verify this. The streamer propagation speed for $r_G = 200$ μm is roughly 1.4 times greater than that for the 25 μm case at $z = 0.1$ cm. The effect on v_s of neglecting diffusion or of varying n_G is much smaller and can be mostly accounted for by a shortened or enhanced SCP, which causes the streamer with no diffusion to enter the FSP earlier and the streamer with $n_G = 10^{12}$ cm^{-3} to enter it later. The double headed streamer case shows the lowest FSP velocity and acceleration.

Current density profiles for several simulation cases are shown in Fig. 24. We show the circuit current calculated in the manner prescribed by Sato [53] and the cathode current. From current continuity the sum of the conduction and induction currents are continuous across the

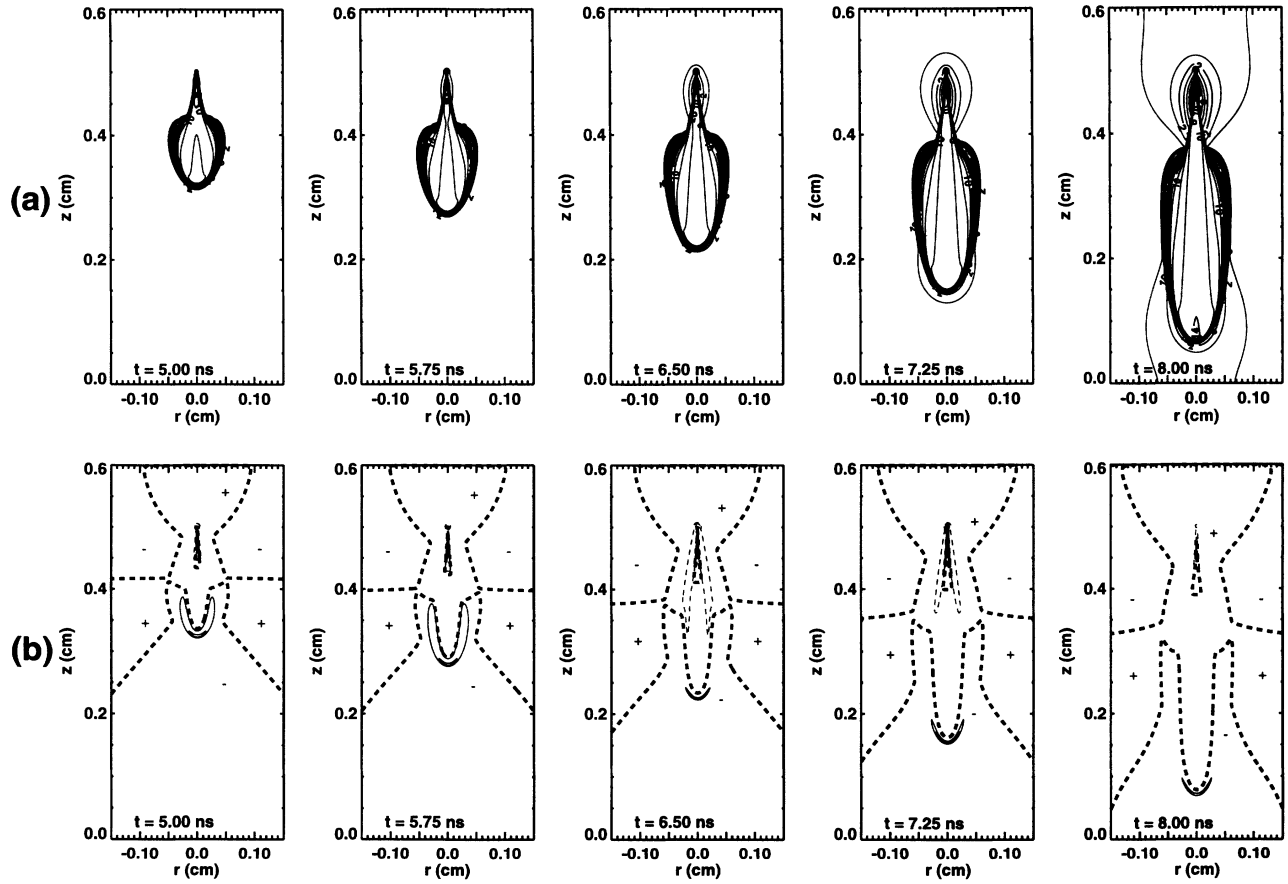

FIG. 21. Contours for a double headed streamer showing the evolution during the FSP of (a) the logarithm of the electron density and (b) the linear space-charge density. The contours of n_e are separated by a factor of 10 in density. For n_s, twenty contours running from the most negative to the most positive value are shown at each time step. Space-charge contours for $n_s > 0$ are shown as dotted curves, while those for $n_s < 0$ are given as thin solid curves. The thick dotted curves correspond to $n_s = 0$ and bound regions where a + or a − designates the sign of the space charge. Initial conditions used were the plane-parallel gap with separation 0.6 cm, fixed voltage 30 kV, $n_B = 10^{-5}$ cm^{-3}, and $r_G = 25$ μm. The Gaussian perturbation was centered on axis at $z = 0.5$ cm.

gap. This continuity should be applied to the cathode current. Just ahead of the streamer the current is primarily due to the induction current. As $I_c \propto v_s E_h / R_h$, where R_h appears to be nearly constant for the models treated here, the variations in the current result from changes in v_s and E_h. Both the streamer propagation speed and the peak electric field increase in magnitude in the FSP from the double peak case to the 200 μm case. In the streamer body the induction current is small and the conduction current is nearly equal to the total current. Since the electric field interior to the streamer body and the e-folding radii are insensitive to initial conditions, the bulk of the observed variation in the conduction current comes from changes in n_e.

V. CONCLUSIONS

The streamers considered in this paper show that even for the simplest plane-parallel electrode configuration a multidimensional, complex morphology develops which changes with time. The streamers pass through multiple phases in their evolution. Starting from an avalanche the streamer passes through an expansion-contraction space-charge phase (SCP) dominated by self-generated space-charge fields. This transient phase precedes the stable filamentary streamer evolution in the filamentary streamer phase (FSP). Other phases occur but were not encountered under the conditions considered in this paper.

Except at the surface, the streamer plasma in the SCP and FSP is quasineutral, with the electron density being tied to the slow moving ion density so as to reduce the space charge. The space-charge density is negative in the streamer body during the SCP, producing a radial space-charge field which pushes electrons outwards radially and axially. With time, the space-charge density becomes positive in the streamer body. The onset of a positive value for space-charge density in the streamer body is one of the structural changes that occurs when the streamer passes from the SCP to the FSP.

During the SCP an enhanced space-charge electric field develops about the streamer head due to shielding. This space-charge field grows in magnitude during the FSP. The drop off from the high peak electric field at the streamer head to the low interior field becomes very sharp as the shielding space-charge layer shrinks in

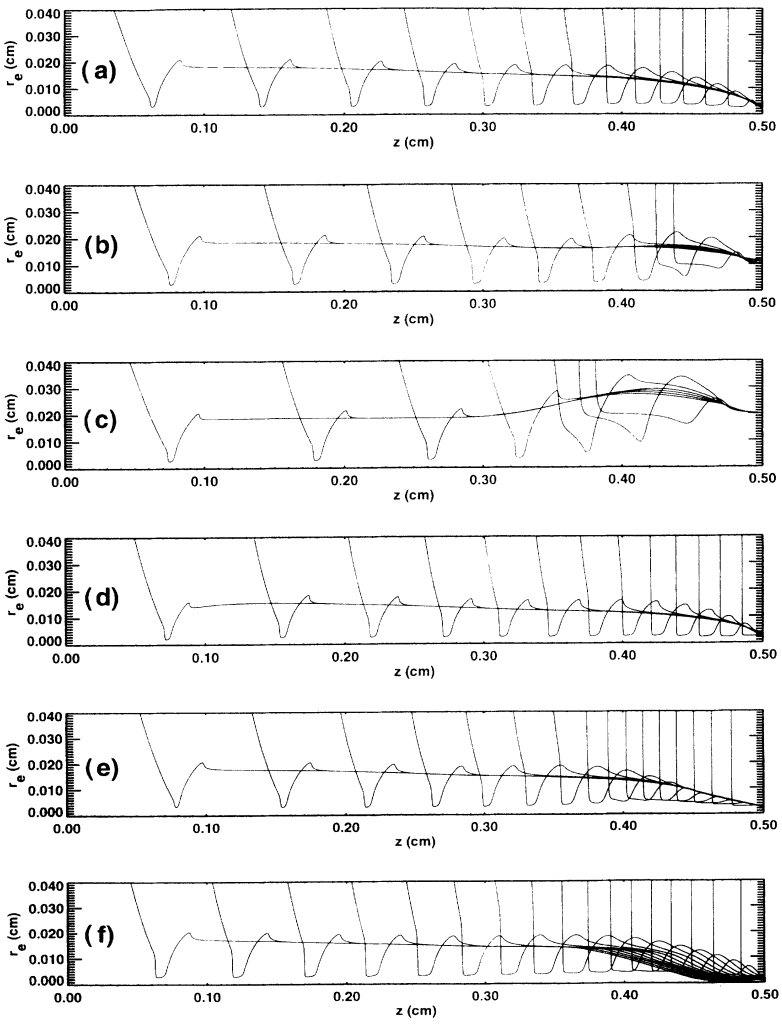

FIG. 22. Evolution of r_e. The effect of varying r_G is shown in (a)–(c) with the corresponding values of r_G being respectively 25 μm, 100 μm, and 200 μm. (d) and (e) give the evolution of r_e when diffusion was neglected and for the initial perturbation density $n_G = 10^{12}$ cm^{-3}. (f) shows r_e for the double headed streamer case. The time spacing between each curve is 0.5 ns. The initial time for the first curve in each figure is respectively 0.25, 0.25, 0.25, 0, 0, 0, ns.

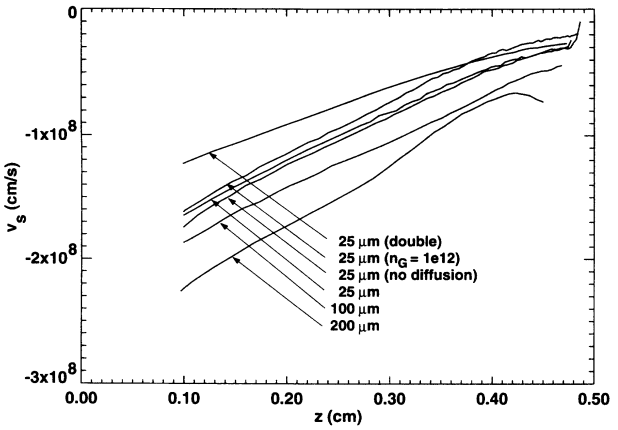

FIG. 23. Streamer propagation velocity as a function of the streamer head position.

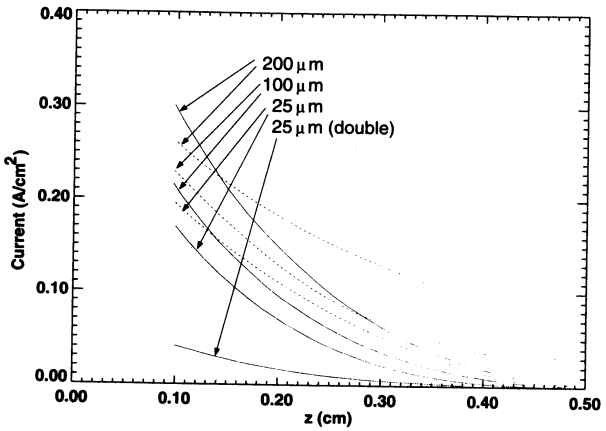

FIG. 24. Current evolution for streamers as a function of axial position. Shown are the circuit currents (solid curves) and the cathode currents (dotted curves).

width, but the drop is smooth when this region is well resolved. For our model conditions we find the electric field on axis behind the streamer head to be shielded to a minimum value of $\simeq 30$ kV/cm. The electric field magnitude rises again in the streamer base until its value is similar to that of the background field.

In the FSP, streamer propagation via an ionization wave is clearly a two-dimensional process, with z displacement close to the axis followed by a rapid radial expansion. The propagation of the streamer does not simply involve an axial displacement of the streamer plasma. For the negative streamers treated in this paper, the values of v_s, n_s, and $|E|$ all increase roughly linearly with length at the streamer head during the FSP, with n_e increasing somewhat faster.

We find that at least two characteristic radii are required to describe the streamer structure in the FSP, which self-consistently forms in our simulations. These length scales correspond to the space-charge shielding radius r_s, and the electron density e-folding radius r_e. While the initial SCP phase is quite sensitive to initial conditions, the streamer structure in the FSP was found to be weakly dependent upon initial conditions over both length scales. We also find that qualitatively there is little difference with and without diffusion for the cases treated.

Our simulation results for negative streamers in N_2 show no sign of quasi-steady-state streamer propagation. The properties of our simulations are weakly dependent upon initial perturbation or background density after the self-consistent radius is formed. We also find that the propagation velocity of negative streamers is not a function of electron density in front of streamer at low densities.

ACKNOWLEDGMENTS

This work was performed under the auspices of the U.S. Department of Energy by the Lawrence Livermore National Laboratory under Contract No. W-7405-ENG-48, with support from the Advanced Energy Projects Division of the Office of Energy Research.

[1] H. Raether, Z. Phys. **112**, 464 (1939).
[2] L. B. Loeb and J. M. Meek, J. Phys. D **11**, 438 (1940).
[3] E. Marode, J. Phys. D **46**, 2005 (1975).
[4] C. Gary, G. Drăgan, I. Lungu, and M. Colteanu, Proc. IEEE **136**, 191 (1989).
[5] H. Isa, Y. Sonoi, and M. Hayashi, IEEE Trans. Electr. Insul. **26**, 291 (1991).
[6] O. Lesaint, P. Gournay, and R. Tobazéon, IEEE Trans. Electr. Insul. **26**, 699 (1991).
[7] P. Rain, C. Boisdon, O. Lesaint, and R. Tobazón, IEEE Trans. Electr. Insul. **26**, 715 (1991).
[8] H. Yamada, T. Murakami, K. Kusano, T. Fujiwara, and T. Sato, IEEE Trans. Electr. Insul. **26**, 708 (1991).
[9] V. P. Gribkovskiĭ, A. A. Gladyshchuk, A. L. Gurskiĭ, E. V. Lutsenko, N. K. Morozova, T. S. Shul'ga, and G. P. Yablonskiĭ, Fiz. Tekh. Poluprovodn. **26**, 1920 (1992) [Sov. Phys. Semicond. **26**, 1076 (1992)].
[10] J. S. Clements, A. Mizuno, W. C. Finney, and R. H. Davis, IEEE Trans. Ind. Appl. **2**, 1183 (1986).
[11] S. Masuda, Pure Appl. Chem. **60**, 727 (1988).
[12] S. Masuda and H. Nakao, IEEE Trans. Ind. Appl. **26**, 374 (1990).
[13] I. Gallimberti, Pure Appl. Chem. **60**, 663 (1988).
[14] B. Eliasson and U. Kogelschatz, IEEE Trans. Plasma Sci. **19**, 309 (1991).
[15] P. A. Vitello, B. M. Penetrante, and J. N. Bardsley, in *Non-Thermal Plasma Techniques for Pollution Control*, edited by B. M. Penetrante and S. E. Schultheis (Springer-Verlag, Heidelberg, 1993).
[16] E. E. Kunhardt and W. W. Byszewski, Phys. Rev. A **21**, 2069 (1980).
[17] J. R. Vaill, D. A. Tidman, T. D. Wilkerson, and D. W.

Koopman, Appl. Phys. Lett. **17**, 20 (1970).
[18] E. D. Lozanskii, Zh. Tekh. Fiz. **38**, 1563 (1968) [Sov. Phys. Tech. Phys. **13**, 1269 (1969)].
[19] G. A. Dawson and W. P. Winn, Z. Phys. **183**, 159 (1965).
[20] I. Gallimberti, J. Appl. Phys. D **5**, 2179 (1972).
[21] É. D. Lozanskiĭ, Usp. Fiz. Nauk. **117**, 493 (1975) [Sov. Phys. Usp. **18**, 893 (1976)].
[22] L. P. Babich, Radiophys. Quantum Electron. **28**, 163 (1985).
[23] J. Wu and E. E. Kunhardt, Phys. Rev. A **37**, 4396 (1988).
[24] A. J. Davies and C. J. Evans, Proc. IEEE **114**, 1547 (1967).
[25] A. J. Davies, C. S. Davies, and C. J. Evans, Proc. IEEE **118**, 816 (1971).
[26] L. E. Kline, J. Phys. D **45**, 2046 (1974).
[27] I. Abbas and P. Bayle, J. Appl. Phys. D **13**, 1055 (1980).
[28] R. Morrow, Phys. Rev. A **32**, 1799 (1985).
[29] R. Morrow, Phys. Rev. A **35**, 1778 (1987).
[30] R. Morrow, IEEE Trans. Plasma Sci., **19**, 86 (1991).
[31] I. Odrobina and M. Černák, Czech. J. Phys. **42**, 303 (1992).
[32] K. Yoshida and K. Tagashira, J. Appl. Phys. D **9**, 485 (1976).
[33] P. Bayle and B. Cornebois, Phys. Rev. A **31**, 1046 (1985).
[34] K. Yoshida, T. Taniguchi, and H. Tagashira, J. Appl. Phys. D **12**, L3 (1979).
[35] A. J. Davies, C. J. Evans, and P. M. Woodison, Comput. Phys. Commun. **14**, 287 (1978).
[36] I. M. Bortnik, I. I. Kochetov, and K. N. Ul'yanov, Teplofiz. Vys. Temp. **20**, 193 (1982) [High Temp. (USSR) **20**, 165 (1982)].
[37] S. K. Dhali and P. F. Williams, Phys. Rev. A **31**, 1219 (1985).
[38] S. K. Dhali and P. F. Williams, J. Phys. D **62**, 4696 (1987).
[39] E. E. Kunhardt and Y. Tzeng, Phys. Rev. A **38**, 1410 (1988).
[40] B. V. Zhuravlev, A. P. Napartovich, A. P. Pal', V. V. Pichugin, A. V. Rodin, A. N. Starostin, T. V. Taran, M. D. Taran, and A. V. Filippov, Fiz. Plazmy **14**, 233 (1988) [Sov. J. Plasma Phys. **14**, 133 (1988)].
[41] M. C. Wang and E. E. Kunhardt, Phys. Rev. A **42**, 2366 (1990).
[42] E. E. Kunhardt and Y. Tzeng, in *Proceedings of the IVth International Symposium on Gaseous Dielectrics,* Knoxville, 1994, edited by L. G. Christophorous (Pergamon, New York, 1984), p. 146.
[43] Y. Tzeng and E. E. Kunhardt, Phys. Rev. A **34**, 2148 (1986).
[44] E. E. Kunhardt, J. M. Penetrante, and J. Wu, Phys. Rev. A **37**, 1654 (1988).
[45] J. Dutton, J. Phys. Chem. Ref. Data **4**, 664 (1975).
[46] S. T. Zalesak, J. Comp. Phys. **31**, 335 (1979).
[47] W. H. Press, B. P. Flannery, S. A. Teukolsky, and W. T. Vetterling, *Numerical Recipes* (Cambridge University Press, Cambridge, 1986).
[48] H. L. Stone, SIAM (Soc. Ind. Appl. Math.) J. Numer. Anal. **5**, 530 (1968).
[49] P. Vitello, C. Cerjan, and D. Braun, Phys. Fluids B **4**, 1447 (1992).
[50] V. A. Davidenko, B. A. Dolgoshein, and S. V. Somov, Zh. Eksp. Teor. Fiz. **55**, 435 (1968) [Sov. Phys. JETP **28**, 227 (1969)].
[51] N. S. Rudenko and V. I. Smetanin, Zh. Eksp. Teor. Fiz. **61**, 146 (1971) [Sov. Phys. JETP **34**, 76 (1972)].
[52] E. D. Lozansky and O. B. Firsov, J. Appl. Phys. D **6**, 976 (1973).
[53] N. Sato, J. Appl. Phys. D **13**, L3 (1980).

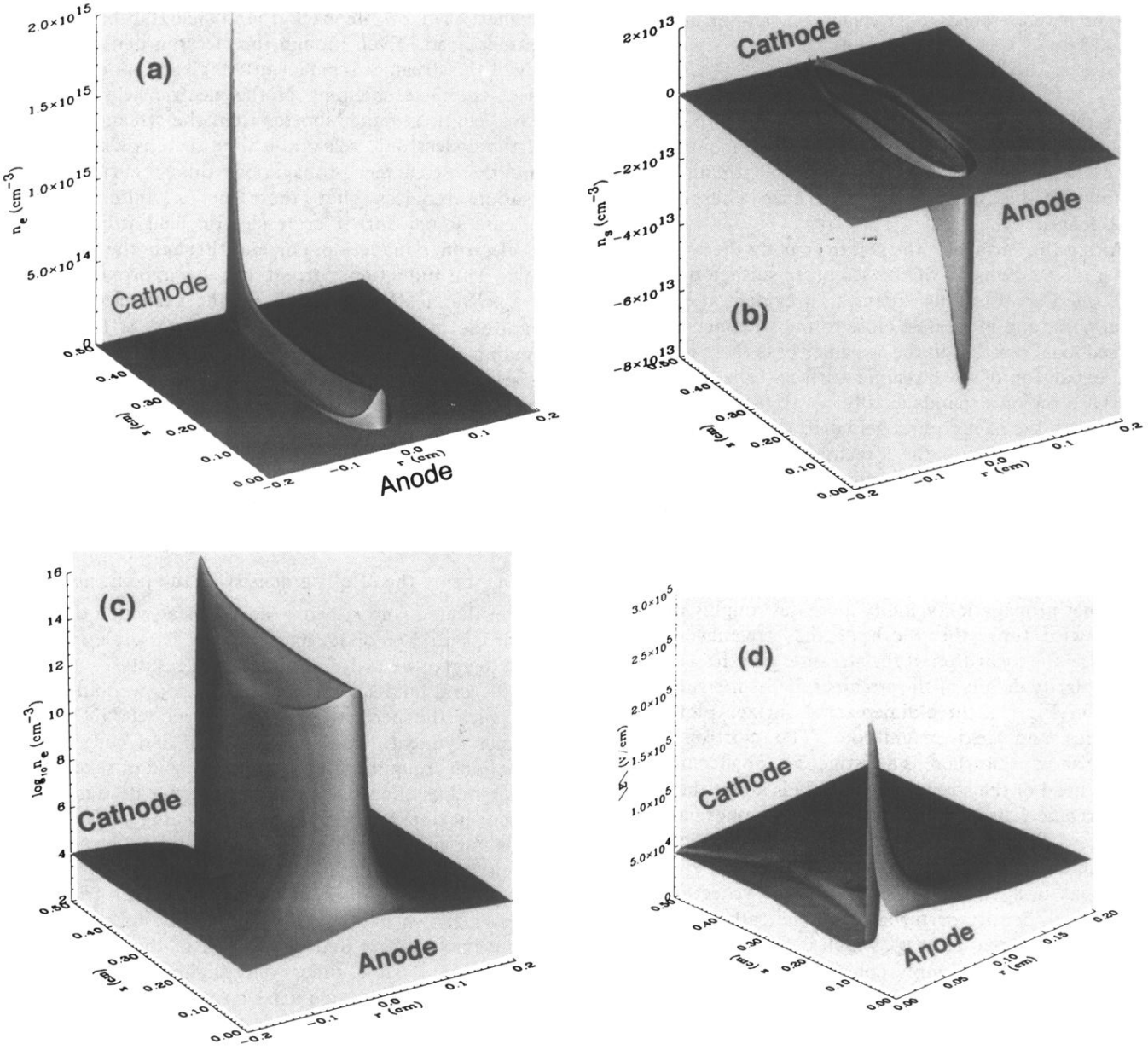

FIG. 12. Details of the filamentary structure for a typical negative streamer during the FSP. The figures show (a) the electron density profile, (b) the space-charge density profile, (c) the logarithm of the electron density profile, and (d) the profile of $|E|$. The profiles correspond to contours given in Fig. 10 at $t = 6.25$ ns.

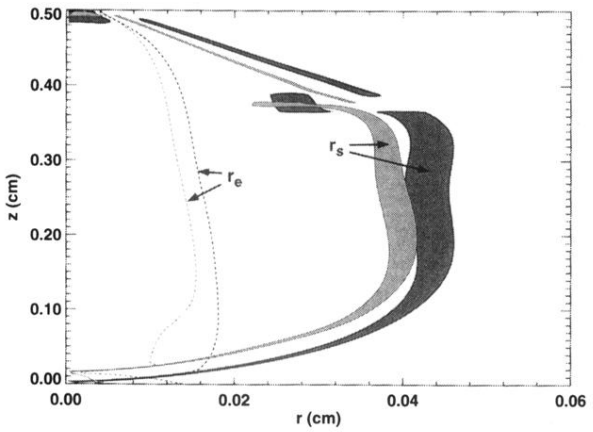

FIG. 16. Profiles of r_e (dotted curves) and r_s (solid contours). The shielding radius is represented by contours at the 90% level of the maximum of $|n_s|$ at each axial point. The thick curve and dark shaded region represent a model simulation including diffusion for $t=6.5$ ns. The thin curve and light shaded region show results neglecting diffusion at $t=6.25$ ns.